# CO<sub>2</sub> Hydrogenation over Rhodium Cluster Catalyst Nucleated within a Manganese Oxide Framework

Shuting Xiang,<sup>1</sup> Juan D. Jimenez,<sup>2</sup> Luisa F. Posada,<sup>3</sup> Samantha Joy B. Rubio,<sup>3</sup> Harshul S. Khanna,<sup>4</sup> Sooyeon Hwang,<sup>5</sup> Denis Leshchev,<sup>6</sup> Steven L. Suib,<sup>3</sup> Anatoly I. Frenkel,<sup>1, 2\*</sup> and Sanjaya D. Senanayake <sup>2\*</sup>

Materials Science and Chemical Engineering Department, Stony Brook University, Stony Brook, NY 11794, USA
 Chemistry Division, Brookhaven National Laboratory, Upton, New York 11973, USA
 Department of Chemistry, University of Connecticut, Storrs, CT 06269, USA
 Institute of Materials Science, University of Connecticut, Storrs, CT 06269, USA
 Center for Functional Nanomaterials, Brookhaven National Laboratory, Upton, New York 11973, USA
 Synchrotron Light Source II, Brookhaven National Laboratory, Upton, New York 11973, USA

#### Abstract

Rhodium-based manganese oxide frameworks were explored as a prototype for carbon dioxide reactive capture and conversion. Three-dimensional frameworks of MnOx were utilized as support structures to isolate Rh metal centers. V, Na, and Zn were introduced as counterions to stabilize the structure and for their beneficial effect as promoters. With this multicomponent catalyst, Rh active centers with MnOxs and varied counterions, we were able to selectively tune the catalytic performance of the material via the choice of counterion and structure of the host material. With cryptomelane-type tunnel manganese oxides octahedral molecular sieve (OMS2), we found that Rh-V-OMS2 was highly stable even after 48 hours on stream with a reaction rate of around 1.5×10<sup>-4</sup> mol CO<sub>2</sub>/g<sub>Rh</sub>/s, surpassing the net reactivity of other initially more active combinations. Furthermore, during CO<sub>2</sub> hydrogenation, in situ XAFS showed that single Rh atoms nucleated into nanoparticles/ sub-nanometer clusters with a coordination number of 5.5 or less. Our finding of the correlation between the reaction rate and particle size offers the potential for enhanced control over the reaction rate by tuning particle size. Our activity study with control experiments demonstrates that the activities of the catalysts are proved due to the unique metal support interaction offered by the Rh-X-MnO.

**Keywords:** CO<sub>2</sub> hydrogenation, Rhodium catalyst, secondary metals, manganese oxide framework, nucleation.

#### 1. Introduction

There is an urgent need to reduce the CO<sub>2</sub> concentration in the atmosphere since CO<sub>2</sub> is the driving factor behind the climate crisis.[1-3] In general, there are four routes to mitigate the CO<sub>2</sub> concentration, including direct reduction of CO<sub>2</sub> emission,[4, 5] CO<sub>2</sub> capture and storage,[6-9] direct utilization of CO<sub>2</sub>,[10, 11] and CO<sub>2</sub> conversion.[12, 13] Among these four routes, the conversion of CO<sub>2</sub> can not only reduce CO<sub>2</sub> emission into the earth's atmosphere but also produce chemicals and energy products with high potential markets.[14] However, CO<sub>2</sub> is kinetically and thermodynamically stable, which is the significant hurdle that prevents CO<sub>2</sub> conversion,[15] which can be reflected by its bond dissociation energy (393.5 kJ/mol).[16] To activate CO<sub>2</sub>, it is necessary to overcome the thermodynamic barrier, requiring active catalysts and adequate reaction conditions for the conversion of CO<sub>2</sub> to value-added products.[11, 17]

To achieve CO<sub>2</sub> conversion, thermal catalysis receives significant attention due to its fast kinetics, flexible combination of active components, and ease of integration into high-yield systems.[18] The hydrogenation of CO<sub>2</sub> primarily produces CO, HCOOH, CH<sub>3</sub>OH, CH<sub>4</sub>, higher hydrocarbons, and oxygenates,[19] which are all entropically disfavored compared to CO<sub>2</sub> and H<sub>2</sub>.[20] For CO<sub>2</sub> hydrogenation, various catalysts are investigated.[21-23] Since altering the catalysts' nuclearity can alter the geometric and electronic properties and the associated reactivity of metal species, there has been increased focus to control the catalysts with increasing atomic

precision.[24-26] Atomically dispersed single-atom active metal sites have attracted attention due to their maximization of atom efficiency, especially for the scarce precious metal atoms. However, for CO<sub>2</sub> hydrogenation, single-atom catalysts generally favor the Reverse Water Gas Shift exclusively.[27-29] Noble metals, such as Ru, Rh, and Pd, are often utilized as effective catalysts for CO<sub>2</sub> hydrogenation.[27, 30, 31] Among the noble metals, Rh is chosen as the primary metal catalyst in this study due to its ability to dissociate H<sub>2</sub> and CO<sub>2</sub>, its excellent activity and chemical stability for CO<sub>2</sub> hydrogenation.[30, 32-35] However, under typical thermal reaction conditions, single atoms on catalysts tend to agglomerate or migrate, and form nanoclusters or nanoparticles.[36, 37] Therefore, the tunning of the size and shape of Rh has been investigated to further control their properties.[38-41]

In our study, we are using a 3D porous manganese oxide structure as the catalyst support, [42] since this highly uniform crystal has its unique porosity, high surface area, rich tunable pore structure, flexibility in shape, and morphologies. [43-45] Additionally, manganese oxide has attracted much attention due to its interesting catalytic properties and wide applications in thermal catalysis. [46] MnOx was used as a promoter for CO<sub>2</sub> hydrogenation previously. [47, 48] Specifically, as shown in Scheme. 1, cryptomelane-type tunnel manganese oxides octahedral molecular sieve (OMS2) and layered birnessite (OL1) were utilized herein. [49] Octahedral layered materials (OL1 or K-OL1) are analogs of the mineral birnessite formed by edge-sharing MnO<sub>6</sub> octahedra resulting in layers or sheets which contain K<sup>+</sup> or Na<sup>+</sup> ions and water molecules in the interlayers. [49] Potassium-containing manganese oxide octahedral molecular sieves (OMS2) are synthetic analogs of naturally occurring tunnel-type manganese oxide mineral cryptomelane. [49] The chemical composition of OMS2 is KMn<sup>4+</sup>7Mn<sup>3+</sup>O<sub>16</sub> • nH<sub>2</sub>O with K<sup>+</sup> cations and H<sub>2</sub>O molecules in the tunnel site. [49] The main difference between OL1 and OMS2 is that OL1 is a

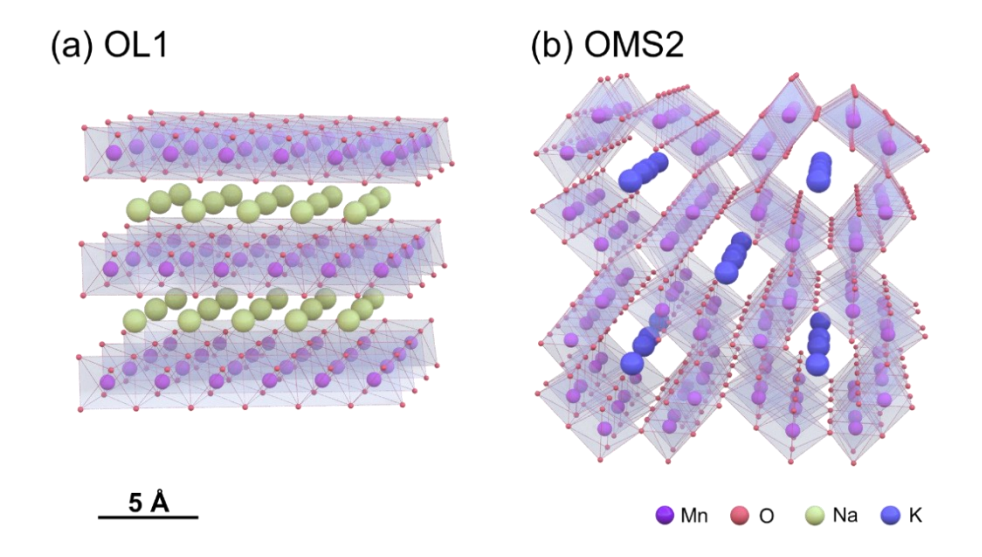
layered structure with the counterion situated between the layers, while OMS2 is a tunnel structure with the counterion situated with the tunnels. Brunauer-Emmett-Teller (BET) surface results of OMS2 (81 m<sup>2</sup>/g) and OL1(43 m<sup>2</sup>/g) have been reported previously.[50] The N<sub>2</sub> adsorptiondesorption isotherms are classified as Type IVa, which is characteristic of mesoporous adsorbents with monolayer-multilayer adsorption followed by pore condensation.[50] Moreover, as previously published, the surface area of multi-doped OMS2 is higher than single-doped OMS2.[51] In this study, we are using the 3D framework of OMS2 and OL1 as the host for our Rh-based catalysts. However, the precise location of the Rh atoms within the OMS2/OL1 structure is not fully understood, where the two possibilities for the location of Rh are: 1) K<sup>+</sup> are replaced by Rh atoms outside the framework of the MnO<sub>6</sub> octahedron, 2) Mn ions in the framework of the MnO<sub>6</sub> octahedron are replaced by Rh atoms. To control the nuclearity of Rh and stabilize the MnOx structure, V was utilized as a counterion in this study. V is also considered an effective promoter in the catalytic process and is known to promote CO dissociation, enhance particle dispersion, limit the sintering of particles, and mitigate coking to subsequently improve the activity of the catalysts with Ni-based nanoparticle catalysts in CO<sub>2</sub> methanation.[52] The successful incorporation of V into the OMS2 framework was reported.[53] To date, the combination of Vpromoted Rh catalyst with atomic dispersion within 3D structural MnO<sub>X</sub> support has not been investigated in the context of CO2 hydrogenation. Additional counterions in the form of Na and Zn were also explored herein due to their known enhancement for CO<sub>2</sub> hydrogenation and thus serve as the control counterions. [54-56] Additionally, Na, Zn, and V can provide different extents of electronic interactions since Na is generally 1+, Zn 2+ and 0, and V 5+/4+. In this study, four sets of combinations of Rh-Na-OL1, Rh-Zn-OL1, Rh-Zn-OMS2, and Rh-V-OMS2 were synthesized, and their structure-function relationship was thoroughly investigated for CO<sub>2</sub>

hydrogenation. The structure of the OL1 and OMS2 cannot be achieved without the counterion, and Na, V, and Zn act as counterions as well instead of only traditional secondary metals. Moreover, the role of Rh and the counterion, including Na, Zn, and V, in Rh-MnOxs is not well-understood in the context of CO<sub>2</sub> hydrogenation. CO<sub>2</sub> hydrogenation is an electron-accepting reaction process, which requires two hydrogen adatoms to convert CO<sub>2</sub> to CO and eight total hydrogen adatoms to form CH<sub>4</sub>, as shown in the following equations:

$$CO_2(g) + H_2(g) \underset{\rightarrow}{\leftrightarrow} CO(g) + H_2O(g)$$

$$CO_2(g) + 4H_2(g) \rightarrow CH_4(g) + 2H_2O(g)$$

For CO<sub>2</sub> methanation over Rh-based catalysts, three possible mechanisms have been proposed: (i) the formate-mediated CO<sub>2</sub> hydrogenation (associative pathway), (ii) the H-assisted CO<sub>2</sub> dissociation followed by CO hydrogenation (RWGS +CO hydrogenation pathway), (iii) the direct dissociation of CO<sub>2</sub> into CO and subsequently into C (direct C-O bond cleavage pathway).[32] Despite many experimental studies on CO<sub>2</sub> hydrogenation over Rh-based catalysts, there is no consensus on the reaction mechanism of CO<sub>2</sub> reduction over Rh-MnOxs.



Scheme 1. Structure of (a) OL1 and (b) OMS2.

Herein, a detailed study of the structure-function relationship for CO<sub>2</sub> hydrogenation over highly controlled Rh sites embedded in MnOx as support was conducted, including the evaluation of catalytic performance, temperature programmed reduction (H<sub>2</sub>-TPR), ex situ and in situ diffuse reflectance infrared Fourier transform spectroscopy (DRIFTS), ex situ X-ray absorption fine structure (XAFS) analysis, in situ XAFS and X-ray diffraction (XRD). In our study, Rh is proven critical to drive the chemistry forward, and the activities of the catalysts are proven due to the unique metal support interaction offered by the Rh-X-MnO. We identified the location of single Rh atoms in the as-synthesized materials and the structure of the Rh clusters under reaction conditions. In our structure-function relationship investigation, we have discovered a significant correlation between the reaction rate and coordination number from the first Rh shell of the particle, an indicator of the particle size, at the beginning stage of the reaction. This correlation offers the potential for enhanced tuning over the reaction rate through the control of particle size. In addition, the observed selectivity of different Rh-MnOxs is consistent with the surface species identified during in situ CO<sub>2</sub> hydrogenation DRIFTS. With spectroscopic understanding coupled with detailed in situ analysis, we find the active site for CO<sub>2</sub> hydrogenation over the Rh-MnOxs catalysts is the Rh cluster sites, while the presence of Rh-X (X=V, Na, or Zn) bonding was not found to be a relevant structural species. Our finding offers further insights into the control of the selectivity of CO<sub>2</sub> reduction toward different products of CH<sub>4</sub> and CO through the utilization of the different combinations of counterion and 3D MnOx structures.

# 2. Experimental Methods

#### 2.1. Materials Preparation

Sodium manganese oxide materials having the synthetic birnessite structure Na-OL1 were synthesized using the reduction method.[57] Tunnel-structured OMS2 materials were fabricated via a reflux method for the oxidation of Mn<sup>2+</sup> by KMnO<sub>4</sub>.[45] Na-OL1 was synthesized by dissolving 6.32 g of KMnO<sub>4</sub> and 48 g NaOH in 400 mL of DI water to make solution A. Then, solution B was made by dissolving 22.48 g MnCl<sub>2</sub>•4H<sub>2</sub>O in 400 mL of DI water. Solution B was added dropwise to solution A with vigorous stirring in an ice bath. The black precipitate was aged at room temperature for 24 h, then washed and dried. The incorporation of Zn was done by ion exchange with a 1M aqueous Zn(NO<sub>3</sub>)<sub>2</sub>•6H<sub>2</sub>O solution for 7 days.

In a typical synthesis for OMS2 materials, 4.43 g of KMnO<sub>4</sub> were dissolved in 75 mL of DI water to make solution A. Solution B was made by dissolving 6.6 g of MnSO<sub>4</sub>•H<sub>2</sub>O in 22.5 mL of DI water, then adding 2 mL of concentrated HNO<sub>3</sub>. Solution A was added slowly to solution B and refluxed for 24 h at 100 °C. The resulting material was washed using copious amounts of DI water, filtered, and dried. Doping of the OMS2 materials was done by adding 30 mL of a 1M solution of the desired dopant into the solution prior to refluxing, using Zn(NO<sub>3</sub>)<sub>2</sub>•6H<sub>2</sub>O or VCl<sub>3</sub> for the incorporation of Zn or V, respectively.

Rh<sup>3+</sup> ion exchanges were performed at 70 °C for 24 h using 1 g of material dispersed in 40 mL of a 0.05 M solution of Rh(NO<sub>3</sub>)<sub>3</sub>•H<sub>2</sub>O. The material was then centrifuged and washed with DI water. After Rh<sup>3+</sup> ion exchange, the materials were dried at 100 °C for 4 hr under air and used as is.

#### 2.2. CO<sub>2</sub> Hydrogenation

Gas phase CO<sub>2</sub> hydrogenation was conducted in a quartz tube reactor secured with quartz plugs. H<sub>2</sub>, CO<sub>2</sub>, and N<sub>2</sub> were used in a ratio of 4:1:1, respectively, at 1 atm pressure with a total

flow of 30 mL/min of the feed gas, with a weight hourly space velocity (WHSV) of 60,000 mL/g<sub>cat</sub>/hr. 30 mg of powder catalysts, sieved to 40-60 microns, were utilized. For experiments at varied temperatures, the catalysts were loaded into the reactor as-synthesized and ramped from 150-450 °C with a ramp rate of 10 °C/min and held at each 50 °C interval for 2 hours to collect 5-6 steady-state measurements per temperature. A GC equipped with TCD/FID effluent analysis, in addition to an on-stream MS for product visualization, was used for the quantification of products. Error was extracted from duplicate measurements. Time on-stream tests were conducted for ~48 hours in an isothermal reactor with H<sub>2</sub>, CO<sub>2</sub>, and N<sub>2</sub> with the ratio of 4:1:1 at 300°C, at 1 atm pressure, with a total flow of 30 mL/min of feed gas, with a WHSV of 60,000 mL·gcat<sup>-1</sup>·hr<sup>-1</sup>. A secondary set of tests was done where an initial H<sub>2</sub> pretreatment was done at 300 °C for 1 hr with a 10 °C/min ramp rate under 10%H<sub>2</sub>/N<sub>2</sub> with a total flow rate of 50 mL/min to probe the effects of the reducing environment on catalytic performance. Following the reduction, CO<sub>2</sub> hydrogenation was run isothermally at 300 °C for 3 hr using the same reaction conditions as listed for the time on stream tests.

#### 2.3. Temperature Programmed Reduction

Prior to measurement, the catalysts were dehydrated in a pure 50 mL/min N<sub>2</sub> flow at 120°C for one hour. After dehydration, the temperature was increased from room temperature to 700°C with a ramp rate of 10°C/min under a flow of 10% H<sub>2</sub> in N<sub>2</sub> with a total flow rate of 50 mL/min. The hydrogen trace, m/z 2, was followed with Mass Spectroscopy using a SRS RGA 100 detector equipped with an electron multiplier, where the m/z 2 trace was allowed to equilibrate for approximately 1 hr at room temperature under 10%H<sub>2</sub>/N<sub>2</sub> prior to measurement to minimize background shifting.

#### 2.4. DRIFTS Measurements

In situ DRIFTS spectra were collected in Kubelka-Munk (K-M) mode using an FTIR spectrometer (Bruker Vertex 70) equipped with a Harrick Praying Mantis cell, an MCT detector, and a mass spectrometer for product visualization (SRS, RGA 100). In situ CO<sub>2</sub> Hydrogenation DRIFTS data was collected at both 200 and 300°C, with corresponding background spectra collected at the specified temperature under He. Feed gas was 4:1:1 of H<sub>2</sub>: CO<sub>2</sub>: He with a total flow rate of 40 mL/min. For CO-DRIFTS, the sample was purged in He for 1 hr, then 10% CO/He was fed for 15 minutes, followed by a He purge for 15 minutes, all at 25°C and 1 atm pressure. All gases used have 99.999% purity.

#### 2.5. X-Ray Absorption Fine Structure Spectroscopy (XAFS)

Ex situ XAFS was conducted at beamline 8-ID (ISS) at NSLS-II. XAFS samples were pressed into 1 mm thick pellets, diluted to ~2 wt% Rh in boron nitride for XAFS analysis with PIPs fluorescence and transmission detector. Rh K-edge, V K-edge, and Zn K-edge data were collected. In situ XAFS was collected at Beamline 7-BM (QAS) at NSLS-II. Nashner-Adler cell was used for in situ CO<sub>2</sub> hydrogenation, as shown in Fig. S1. Catalyst was pressed into 1 mm thick pellets. A gas mixture of 4:1:1 ratio of H<sub>2</sub>: CO<sub>2</sub>: He with 30 mL/min total flow rate ran through the system. The temperature was increased from RT to 200°C at 10°C/min and stayed at 200°C for one hour. After one hour at 200°C, the temperature was increased to 300°C at 10°C/min and then reduced to RT. Rh foil data was collected for calibration in tandem using the reference ionization detector. XAFS data at Rh K-edge were collected during this process from RT before reaction to the end for each of these Rh-MnOxs catalysts.

#### 2.6. Powder X-Ray Diffraction (XRD)

X-Ray diffraction was carried out using a Rigaku Ultima powder X-Ray diffractometer using a Cu k-α (1.54 nm) operated at 40 kV and 44 mA.

# 2.7. Transmission Electron Microscopy (TEM) and Elemental Distribution Mapping (TEM-EDS)

Transmission electron microscopy imaging was done by depositing the catalysts onto Cu grids via drop-casting and drying the resultant material onto the grid. Images were collected on a FEI Talos F200X at an accelerating voltage of 200 kV.

#### 3. Results and Discussion

#### 3.1. Structure and morphology of Rh-X-(OL1/OMS2)

The loading of Rh and the counterion varies between OMS2 and OL1, as shown in Table. S1, due to the intrinsic differences in the extent of Rh and counterion needed to maintain the structure of the material. As-synthesized OL1 samples, Rh-Na-OL1 and Rh-Zn-OL1, had morphologies of sheet, based on the scanning transmission electron microscope (STEM) images shown in Fig. 1(a), Fig. S2(a) and (b). The as-synthesized OMS2 samples, Rh-Zn-OMS2 and Rh-V-OMS2, had only one wire morphology, as shown in Fig. 1(b), Fig. S2(c) and (d). In both OL1 and OMS2 samples, Rh and all other species were well-dispersed over the 3D MnO<sub>X</sub> structure, based on the element mapping images in Fig. S3 to Fig. S6.

In the as-synthesized OL1 samples, there was the crystalline structure of the birnessite-MnO<sub>2</sub>, a typical layered manganese oxide structure, since only peaks characteristic for birnessite-MnO<sub>2</sub>[56, 58, 59] were observed from XRD, as shown in Fig. 1(c) and 1(d). There were crystalline diffraction peaks from tetragonal cryptomelane composed with MnO<sub>2</sub> octahedra in all Rh-OMS2 samples since only the peaks characteristic for OMS2[51, 60-62] were observed, as shown in Fig. 1(e) and 1(f). The coexistence of MnO<sub>2</sub> of birnessite and cryptomelane has been shown in other comparable systems using OMS2 and OL1 materials for various types of reactive systems, where the macrostructure of birnessite and cryptomelane yields multiple diffraction peaks. These results imply that the crystalline structures of birnessite in OL1 and cryptomelane in OMS2 were well preserved with the mixing of Rh and counterions.[60] The fact that no additional peaks assigned to other crystalline phases were detected suggested that the Rh and counterions were incorporated into the birnessite matrix in OL1 and the cryptomelane matrix in OMS2.[60]

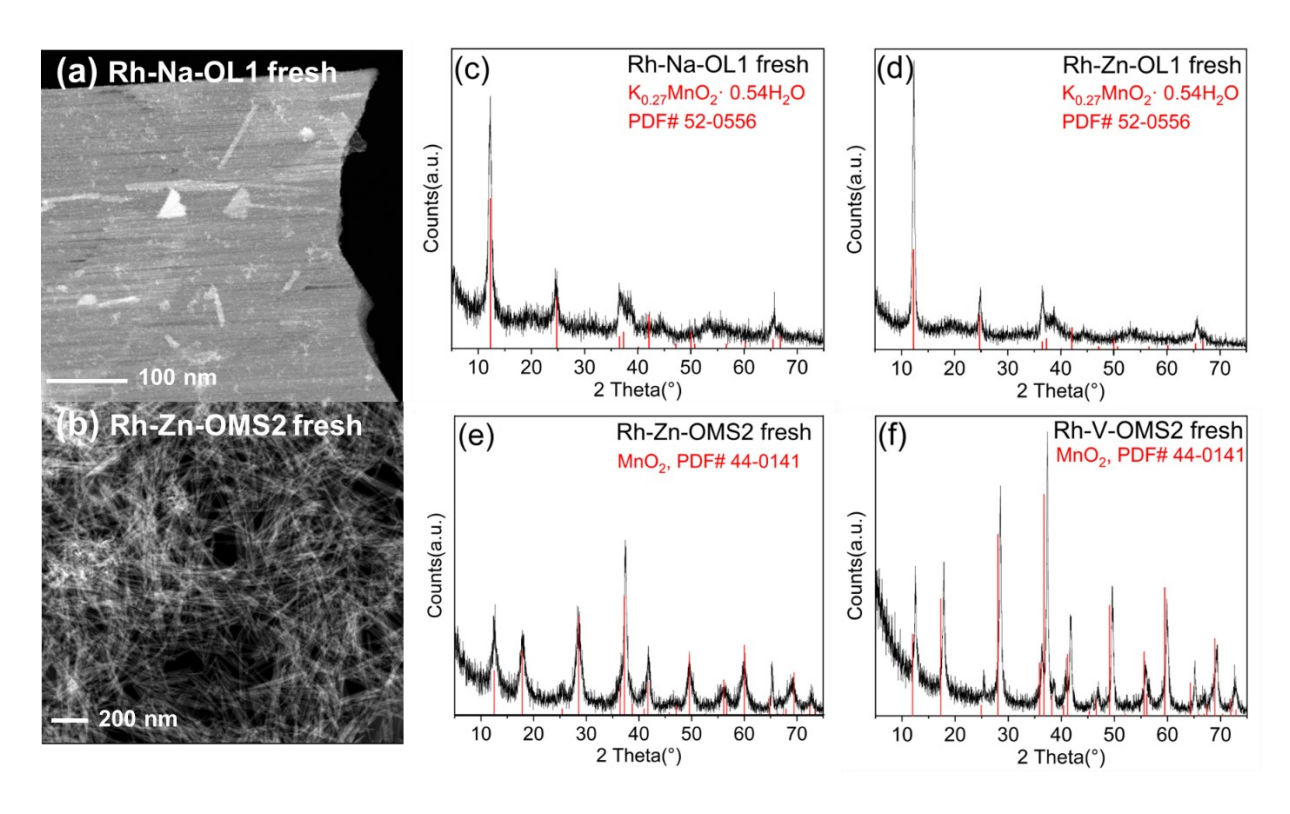


Figure 1. TEM images of as-synthesized (a) Rh-Na-OL1 and (b) Rh-Zn-OMS2. XRD results for the as-synthesized samples of (c) Rh-Na-OL1, (d) Rh-Zn-OL1, (e) Rh-Zn-OMS2, and (f) Rh-V-OMS2.

#### 3.2. Catalytic Performance of Rh-X-(OL1/OMS2)

The catalytic performance of CO<sub>2</sub> hydrogenation was evaluated over the Rh-based catalysts and shown in Fig. 2. The CO<sub>2</sub> conversion and the selectivity towards CH<sub>4</sub> and CO are shown over a temperature range of 150-450 °C, where the carbon balance for all tests is closed to unity. Rh-V-OMS2 yielded a high selectivity towards CO of ~90% from 200°C to 450°C. Comparing different MnOxs support, Rh-Zn-OL1 in Fig.2(d) and Rh-Zn-OMS2 in Fig. 2(b), Rh-Zn-OL1 gave higher CH<sub>4</sub> selectivity, showing that OL1 promotes the diffusion of H<sub>2</sub> to form higher hydrogenated products in the form of CH<sub>4</sub> instead of CO. Comparing between OL1 samples, Rh-Na-OL1 and Rh-Zn-OL1, Rh-Na-OL1 has the highest CH<sub>4</sub> selectivity of 98% at 250°C, and Rh-Zn-OL1 has a main CO selectivity and highest of 95% at 450°C instead. There were distinct

differences in product selectivity based on the counterion species, indicating that the nature of the active site is heavily influenced by the counterion, showing that its influence goes beyond structural effects. Zn is known to be a beneficial promoter for the dissociative CO<sub>2</sub> hydrogenation pathway, resulting in the formation of methoxy and CO intermediates that are favorable to methanol formation,[63] while Na is known to favor methanation and is a well-known promoter for CO<sub>2</sub> hydrogenation.[64, 65] For Rh-V-OMS2, Rh-Zn-OMS2, and Rh-Zn-OL1, the CO<sub>2</sub> hydrogenation favors CO production, supporting the RWGS+ CO pathway proposed for the CO<sub>2</sub> hydrogenation for these three samples. Additionally, in the absence of Rh active sites, the baseline V-K-OMS2 and Zn-K-OMS2 show negligible catalytic performance for CO<sub>2</sub> hydrogenation (Fig. S7), which means the Rh is critical to drive the chemistry forward and changes in the activity as a function of counterion can be attributed to Rh synergies under reaction conditions.

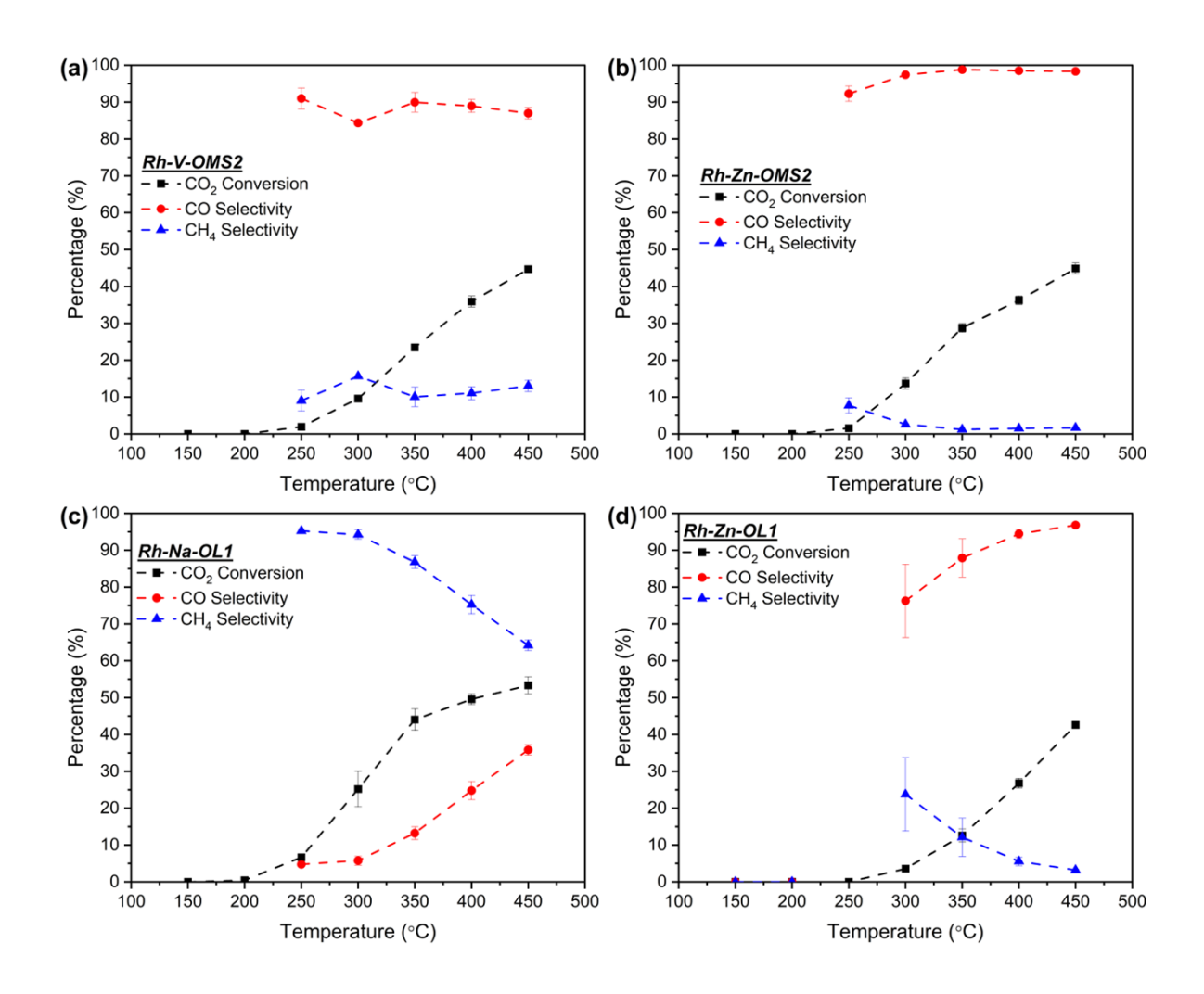


Figure 2. CO<sub>2</sub> hydrogenation from 150-450 °C of (a) Rh-V-OMS2, (b) Rh-Zn-OMS2, (c) Rh-Na-OL1, and (d) Rh-Zn-OL1. Conditions: 4:1:1 of H<sub>2</sub>: CO<sub>2</sub>: N<sub>2</sub> feed composition, 30 mg catalyst, 60,000 mL/gcat/hr WHSV, 30 mL/min total flowrate, 1 atm pressure, GC equipped with TCD/FID effluent analysis.

#### 3.3. Reducibility of Rh-X-(OL1/OMS2)

As CO<sub>2</sub> hydrogenation is a highly reducing environment, to understand the reducibility of our catalysts and to find the most efficient reduction conditions for CO<sub>2</sub> hydrogenation, H<sub>2</sub> temperature programmed reduction (H<sub>2</sub>-TPR) was conducted. The data collected from the samples are shown in Fig. 3. The peak around 100°C is attributed to the reduction of well-dispersed Rh<sub>2</sub>O<sub>3</sub>,

signaling the transition from Rh<sup>3+</sup> to Rh<sup>0</sup>.[66-70] From Fig. 3, the reduction temperatures of Rh-MnOxs are in the order of Rh-Zn-OL1 < Rh-Na-OL1 < Rh-Zn-OMS2 < Rh-V-OMS2. Notably, all the catalysts show a reduction feature < 100°C followed by a more pronounced reduction event at ~120 °C, where this event is due to the reduction of highly dispersed RhOx species. The broad shoulder centered at approximately 140°C is attributed to the reduction of the MnO<sub>2</sub>, the supporting material, via the excess spillover of the activated hydrogen from the metallic rhodium.[71] In the absence of Rh, the base OMS2 materials show a reduction temperature of approximately 300°C, where the Zn-K-OMS2 is more reducible than the V-K-OMS2, the latter showing a secondary reduction event at 350°C (Fig. S8). This low temperature of MnO<sub>2</sub> reduction indicates there is a strong metal support interaction between Rh and MnOxs with readily available hydrogen spillover.[71, 72] However, the reducibility of Rh is mostly governed by the nature of the supporting OL1 or OMS2, where both OMS2 catalysts yield a comparable trend, similarly for both OL1 species, which suggests the mobility of H2 species is influenced by the ordered structure of the base support. Both OL1 samples were reduced at a lower temperature, therefore showing OL1 is more reducible than OMS2. Additionally, a broadband reduction was observed above 200 °C, which may be due to the aggregation of MnO species or the growth of Rh particles. The fact that there was no broadband above 200°C in Rh-V-OMS2, compared with other Rh-MnOxs, suggests minimal aggregation of MnO in the ordered structure of Rh-V-OMS2.

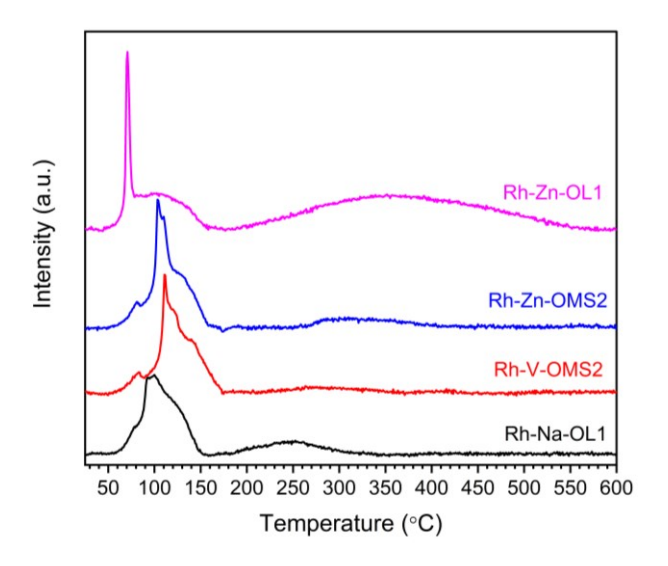


Figure 3. Hydrogen temperature programmed reduction (H<sub>2</sub>-TPR) over the Rh-MnOx catalysts. Conditions: 10%H<sub>2</sub>/N<sub>2</sub>, 50 mL/min total flow, 100mg catalysts, 120 °C in pure N<sub>2</sub> dehydration for 1hr pretreatment, 10 °C/min ramp rate, utilizing a Mass Spectrometer detector following hydrogen (m/2=2) consumption.

#### 3.4. Extended Time-on-Stream CO<sub>2</sub> Hydrogenation

The stability of the catalyst during reaction is a key parameter to evaluate the performance of the catalyst. To understand the stability of the catalysts, a time-on-stream test was conducted at 300°C for 48 hours, as this temperature showed the most promising differences between the catalysts. Based on the stability tests shown in Fig. 4(a), Rh-V-OMS2 had the highest stability in both the overall reaction rate and the product distribution over the whole 48 hours shown in Fig. 4(b). This phenomenon can be explained by the more stable structure provided by the combination of Rh, V, and OMS2 compared with other samples, as shown in Fig. S9. As shown in Fig. S10, the elemental distribution of all species in Rh-V-OMS2 remained well intact, compared with other Rh-MnOxs, which showed more considerable change in the structure shown from Fig. S11 to S13. Additional tests were done where an initial H<sub>2</sub> pretreatment was done at 300 °C for 1 hr prior to the reaction to probe the direct influence of changing the structure of the materials before reaction,

as shown in Fig. S14. The H<sub>2</sub> pretreatment had no discernable influence on the catalytic performance for all catalysts and was within the error of the original as-synthesized reaction runs. However, the H<sub>2</sub> treatment was sufficient to change the ordered structure of all materials into the base MnO structure, as shown in XRD results in Fig. S15, showing the root differences in the catalysts are not due to the transition of ordered structure to MnO, but rather the unique metal support interactions offered by the Rh-X-MnO moiety.

Compared with Rh-V-OMS2, Rh-Zn-OMS2 initially showed a stable reaction rate, then a sharp decline in activity around 20 hr shown in Fig. 4(a), which is likely due to the slow formation of a MnCO<sub>3</sub> species as CO<sub>2</sub> hydrogenation can gradually build up carbon (Fig. S15). As a reference sample with a low concentration of Na, Rh-Na-OL1 shows a sharp decline in reactivity upon the first 12 hours, where post-reaction STEM imaging shows an average particle of only ~1.9 nm, showing that the loss in activity is likely not due to appreciable particle size growth. However, the loss of activity is likely due to the rapid incorporation of CO<sub>2</sub> into the host structure, shown by the formation of MnCO<sub>3</sub> in the post-reaction diffraction, where Na has a strong affinity to capture and incorporate CO<sub>2</sub> into its lattice. The H<sub>2</sub> pretreatment test also reveals that the loss of activity is not due to the structural changes of the material, where the OL1 structure was already converted into MnO after pretreatment, as shown in Fig. S15, and an identical trend in deactivation was still observed, showing it is unique to the reaction conditions. Rh-Zn-OL1 showed the lowest net reactivity among all catalysts, with a corresponding activity after the H<sub>2</sub> pretreatment. However, Rh-Zn-OL1 did not form a distinct MnCO<sub>3</sub> phase, showing no carbon incorporation into the lattice. However, while the net reactivity of Rh-Zn-OL1 was low, it possessed remarkable stability, showing only a nominal decrease in reaction rate after 48 hr. While all catalysts show a nominal particle size distribution of about  $1.8 \pm 0.2$  nm of Rh, as shown in Fig. S16, all of the counterion

and additional elements present in the OMS2/OL1 catalyst remain highly dispersed, showing no aggregation for any species (Fig. S10-13). Furthermore, to show that the system is not mass transfer limited, a Weisz Prater Criterion analysis was performed (shown in Supplemental Information), where the criterion was satisfied, verifying that none of the catalyst are limited by internal mass transfer at any point during the reaction.

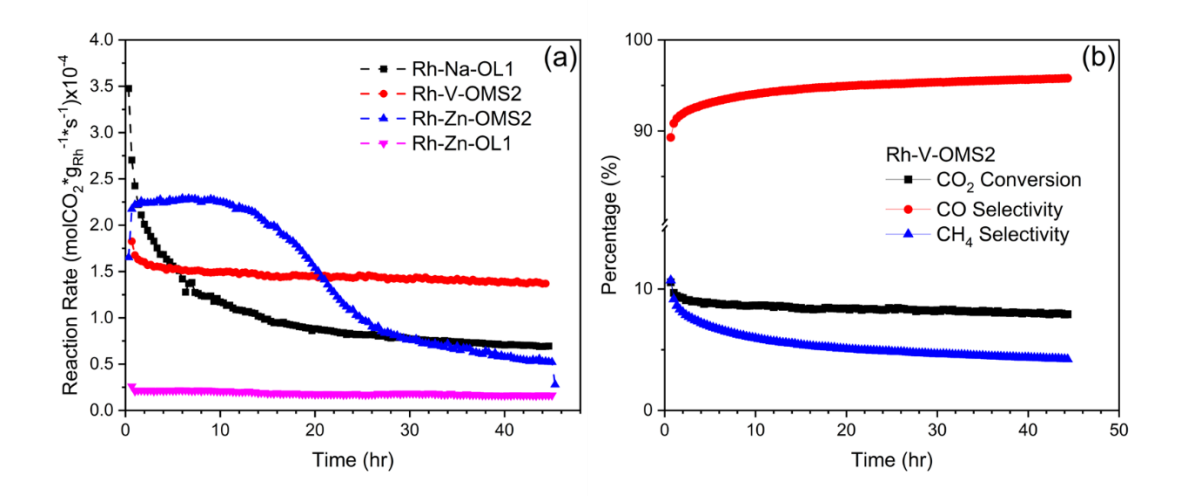


Figure 4. Stability test results for Rh-X-MnOx following (a) the rate of CO<sub>2</sub> reaction normalized to rhodium content and (b) Product distribution of Rh-V-OMS2 over the stability test showing CO<sub>2</sub> conversion and individual CO and CH<sub>4</sub> selectivity. Conditions: 300°C isothermal reactor, 4:1:1 of H<sub>2</sub>: CO<sub>2</sub>: N<sub>2</sub> feed composition, 30 mg catalyst, 60,000 mL/gcat/hr WHSV, 30 mL/min total flow rate, 1 atm pressure, GC equipped with TCD/FID effluent analysis.

### 3.5. Surface Carbonyl Chemistry over Rh-X-(OL1/OMS2)

To understand the surface chemistry of the material under controlled reaction conditions, diffuse reflectance infrared Fourier transforms spectroscopy (DRIFTS) was utilized.[73-75] CO-DRIFTS studies were carried out to investigate the adsorption sites on Rh species over the Rh-MnOx catalysts. The DRIFTS results for Rh-MnOxs are shown in Fig. 5. The peak around 2110 cm<sup>-1</sup> is assigned to the adsorption of CO on atop-Rh<sup>2+</sup> species.[76] The peaks at 2095 and 2018 cm<sup>-1</sup> can be assigned to the absorption of symmetric and asymmetric CO dimer on Rh<sup>+</sup>,

respectively.[76] The absence of the peak from Rh<sup>0</sup> in Rh-V-OMS2, Rh-Na-OL1, and Rh-Zn-OL1 indicates that Rh atoms were highly dispersed and cationic in these three samples. In the case of Rh-Zn-OMS2, there is a slight formation of atop Rh<sup>0</sup> CO binding at 2055 cm<sup>-1</sup>, which is likely attributed to the reduction of the Rh under CO environment, as shown in Fig. 5, where minority defect Rh<sub>2</sub>O<sub>3</sub> species can be readily reduced by CO to form trace Rh<sup>0</sup>-CO atop sites. While all catalysts possess the Rh<sup>2+</sup> and Rh<sup>1+</sup>, albeit in distinct ratios, both OMS2-based catalysts show slight metallic Rh<sup>0</sup> species. This is likely the reduction of unstable rhodium oxide species situated in defect sites, while the OL1 catalysts show only Rh<sup>2+</sup>/Rh<sup>1+</sup> species. The presence of both Rh<sup>2+</sup> and Rh<sup>1+</sup> suggests a bimodal distribution of Rh, where Rh<sup>1+</sup> species are generally attributed to highly dispersed single-atom Rh species, while Rh<sup>2+</sup> may result from small clusters of rhodium oxide.

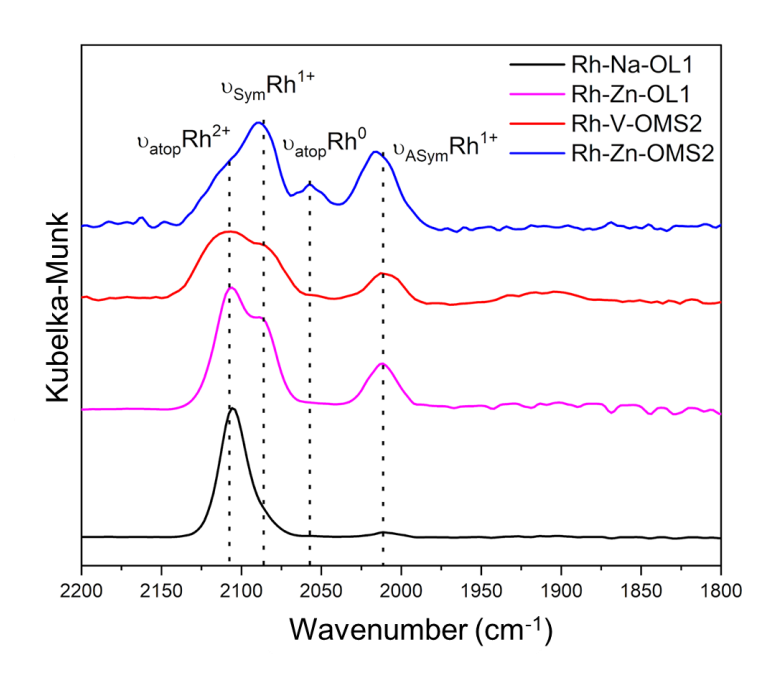


Figure 5. CO Adsorption DRIFTS over Rh-MnOxs after He purge. Conditions: 10% CO/He feed for 15 minutes followed by He purge for 15 minutes, 50 mL/min total flow, 25 °C, 1 atm, 4cm<sup>-1</sup> resolution, MCT detector.

#### 3.6. Structural Analysis of as-synthesized Rh-X-(OL1/OMS2)

To extract the structure of the as-synthesized materials, ex situ XAFS spectra were collected. Rh K-edge data were collected. As shown in Fig. 6(a), there is an apparent deviation between the XANES spectra of Rh-MnOxs samples and XANES of Rh foil, indicating the obvious oxidation of Rh atoms in the catalysts. As shown in Fig. 6(a), the edges of Rh-MnOxs are at the same position as Rh<sub>2</sub>O<sub>3</sub>, indicating Rh-MnOxs have the same oxidation number as Rh<sub>2</sub>O<sub>3</sub>. These results are distinct from CO-DRIFTS due to the fact that CO induces surface reduction, while XAFS is a bulk technique, and the fact that Rh<sup>3+</sup>/Rh<sup>4+</sup> does not show strong CO bindings modes at room temperature.

From the R-space spectra of the four Rh-MnOx samples in Fig. 6(b), the first peaks from Rh-MnOxs are at the same position as the Rh-O peak of Rh<sub>2</sub>O<sub>3</sub>, suggesting that the first shell of Rh-MnOxs is Rh-O. Additionally, before EXAFS fitting, to further confirm the bond type in the samples, wavelet transform (WT) was applied to the spectra from Rh-MnOxs, Rh foil, and Rh<sub>2</sub>O<sub>3</sub> as references. Wavelet transform is a powerful technique, inherited from the signal processing field, for the identification of the overlapped contributions coming from different neighbor atoms, since if two or more groups of different atoms are localized at close distances around the absorber, their contributions in the direct space R overlap, becoming indistinguishable.[77-79] As the WT results shown in Fig. S17, the first two features around 1.5 Å from Rh-MnOx samples are similar to the ones from Rh<sub>2</sub>O<sub>3</sub>. This result indicates that the first shell from Rh-MnOx samples is the same as in Rh<sub>2</sub>O<sub>3</sub>, which is Rh-O. Therefore, Rh-O path was used in EXAFS fitting for the first shell. From EXAFS fitting, the coordination numbers (CN) of Rh-O from the first shell of all Rh-MnOxs are consistent with 6-7 for all Rh-MnOx samples, as shown in Table 1. This result provided support for the hypothesis that Rh atoms were replacing the Mn ions in the MnO<sub>6</sub> octahedral structures. Insertion of precious metals, such as Co, Ag, Ru, and Pt have all been reported to

substitutionally inserted into MnO<sub>2</sub> octahedron within OMS-2 heterostructures[80-84] within the OMS-2 structure. The K<sup>+</sup> is not likely to be replaced within the framework due to the mismatch of the size difference between Rh<sup>3+</sup> (0.67 Å) and K<sup>+</sup> (1.65 Å). However, the differences between Rh and Mn are much more comparable at 0.67 Å and 0.67-0.72 Å for Rh<sup>3+</sup> and Mn<sup>(4+)</sup>, respectively.[80] For the second shell, EXAFS fitting of Rh-Rh, Rh-Mn, Rh-Zn, and Rh-V for corresponding samples was discussed in detail in Note S1. in the supporting information. Based on the EXAFS fitting results (Rh-Rh model was the worst) and the concentration of the elements in the fresh sample (Zn and V are minority elements relative to Mn), Rh-Mn was proposed to be the most reasonable model for the second shell. The EXAFS fitting utilizing this model supports the claim that Rh is well dispersed in the MnOx, as shown in Fig. S19 and Table 1. However, the possibility of highly dispersed RhOx species existing outside of the MnOx heterostructures cannot be ruled out solely by EXAFS. The relatively low values of the Rh-Mn mean square displacements and coordination numbers (Table 1) are their lower bounds due to the correlation of these quantities in the fit.

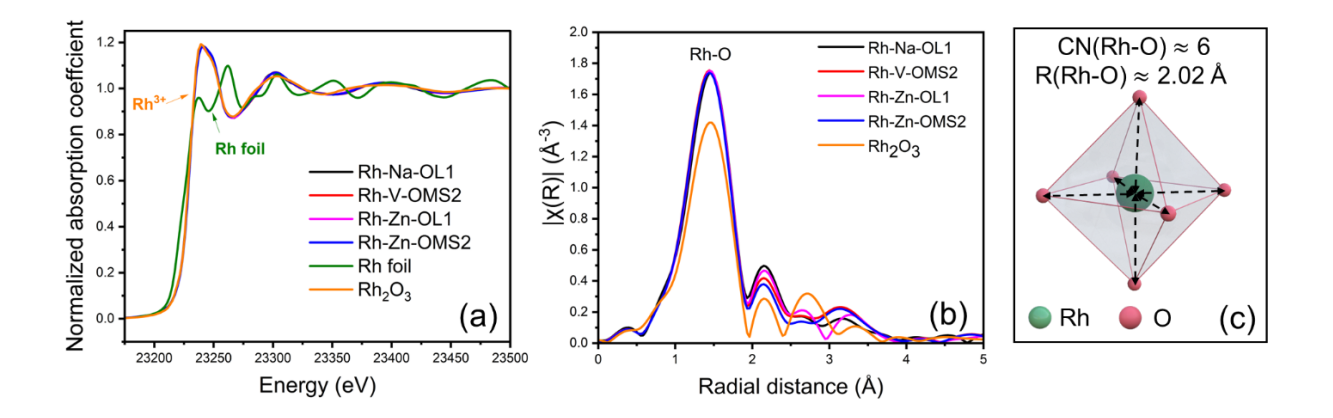


Figure 6. (a) XANES spectra for Rh K-edge of Rh-MnOxs. (b) R-space spectra for Rh K-edge. (c) Scheme of Rh inside oxide octahedra framework.

Table 1. EXAFS fitting results for pristine Rh-X-MnO<sub>X</sub>. Uncertainties in the last significant digits are given in parentheses.

Rh K-edge							
Sample Name	Contributions	CN	R(Å)	$\sigma^2 (\mathring{A}^2)$	ΔE (eV)	Reduced χ <sup>2</sup>	R-factor
Rh-Na-OL1	Rh-O	6.3(6)	2.02(1)	0.0016(7)	-1.4(1.1)	42	0.03
	Rh-Mn	1.0(5)	2.92(1)	0.0001(23)			
Rh-Zn-OL1	Rh-O	6.6(6)	2.02(1)	0.0025(8)	-1.1(1.2)	1028	0.03
	Rh-Mn	0.9(6)	2.92(2)	0.0006(28)			
Rh-Zn-OMS2	Rh-O	6.6(6)	2.02(1)	0.0026(8)	-1.1(1.1)	2137	0.02
	Rh-Mn	0.6(5)	2.92(2)	0.0008(40)			
Rh-V-OMS2	Rh-O	6.6(6)	2.02(1)	0.0027(8)	-1.1(1.1)	2234	0.02
	Rh-Mn	0.9(6)	2.92(2)	0.0014(34)			
			Zn K-	edge			<u> </u>
Rh-Zn-OL1	Zn-O	6.4(4)	2.02(1)	0.0088(12)	1.8(7)	1199	0.002
Rh-Zn-OMS2	Zn-O	6.5(5)	1.99(1)	0.0077(13)	1.1(8)	146	0.003

<sup>\*</sup> Rh K-edge:  $2.0 \le k \le 16 \text{ Å}^{-1}$ ,  $\Delta k = 2.0 \text{ Å}^{-1}$ ,  $1.0 \le R \le 2.85 \text{ Å}$ . Zn K-edge:  $2.0 \le k \le 12 \text{ Å}^{-1}$ ,  $\Delta k = 2 \text{ Å}^{-1}$ ,  $1.0 \le R \le 4.0 \text{ Å}$ .

To extract the structural information of the counterion, XAFS data from V K-edge and Zn K-edge were also collected. To determine quantitative and accurate oxidation state and symmetry information for vanadium, correlations between normalized pre-edge peak area and its centroid position have been identified as the most reliable method.[85, 86] Based on Fig. S20(f), V atoms in Rh-V-OMS2 have a similar oxidation number of 4<sup>+</sup>, consistent with previous literature,[46] and

a similar octahedral structure with VO<sub>2</sub>. This result suggests that V atoms were also replacing Mn atoms in the MnO<sub>6</sub> octahedral structures. Rh-Zn-OL1, Rh-Zn-OMS2, as well as reference ZnO, and Zn foil were measured at Zn K-edge. From their XANES spectra in Fig. S20(b), Rh-Zn-OL1 and Rn-Zn-OMS2 have higher oxidation numbers than ZnO since the edge positions of these two samples are on the right of the edge of ZnO. The features of XANES of fresh Rh-Zn-OL1 and Rh-Zn-OMS2 from Zn K-edge differ greatly from ZnO. Because we could not extract the second shell (Zn-Mn or Zn-Zn) information reliably from the Zn EXAFS data, we limited the EXAFS analysis to the first shell only (Zn-O contributions). The EXAFS fitting results are shown in Table 1 and Fig. S21(a) to (d). The coordination number in the first shell of Zn-O from EXAFS fitting is around 6 in all Zn samples, suggesting the Zn is insert into MnO<sub>2</sub> octahedron within OMS-2 heterostructures. Additional details are discussed in the supporting information Note S1.

#### 3.7. In situ Extended Fine Structure of Rh-X-(OL1/OMS2)

To track the local structure change surrounding the absorbing atoms during CO<sub>2</sub> hydrogenation, in situ XAFS data were collected for these catalysts. In Fig. 7, the spectra from red to yellow are the in situ XANES spectra from the beginning to the end of the reaction. The green spectrum is from Rh foil. From Fig. 7, a clear change in the spectra towards metallic Rh during CO<sub>2</sub> hydrogenation throughout the process for all Rh-MnOxs is observed. Fig. S22 shows the EXAFS spectra during the process, with K-space spectra shown in Fig. S23. Rh-O bonds were fully reduced in all samples at the end of the reaction, and Rh-Rh bonds increased, confirmed by the EXAFS fitting results shown in Fig. S24 and Table. S3 to Table S6. As shown in Fig. 8, the number of Rh-O bonds in Rh-MnOxs reduced from around 5.5 to zero, indicating that all the samples were fully reduced after reaction. The number of Rh-Rh bonds in Rh-Na-OL1 increased to around 5.5 after the reduction, suggesting that the nucleation of Rh atoms happened during the

reduction. Since there was no oxygen left in the sample, the number of Rh atoms was the total number of atoms in the nanoparticle, which suggests a homogeneous material. Therefore, the coordination number in the nanoparticles is the total metal-metal coordination number.[87] Based on the correlation between the coordination number and the number of atoms in the most commonly used nanoparticles, when the coordination number of the first layer is around 5.5, the number of atoms in the nanoparticle was calculated to be 13.[88] Since there is a positive correlation between the coordination number of the first shell and the number of atoms, when the coordination number is less than 5.5, the number of atoms in the cluster should be less than 13. In Rh-Zn-OL1 and Rh-Zn-OMS2, the CN of Rh-Rh increased to 3.1 and 4.0 correspondingly, indicating Rh atoms nucleated into sub-nanometer clusters at the end of the reaction. The coordination number extracted from in situ XAFS are indicative of the true particle size under reaction conditions, where post-reaction XRD and STEM show high dispersion after the catalyst was exposed to air after reaction, where Rh is highly oxophilic and likely immediately oxidized in the presence of air.

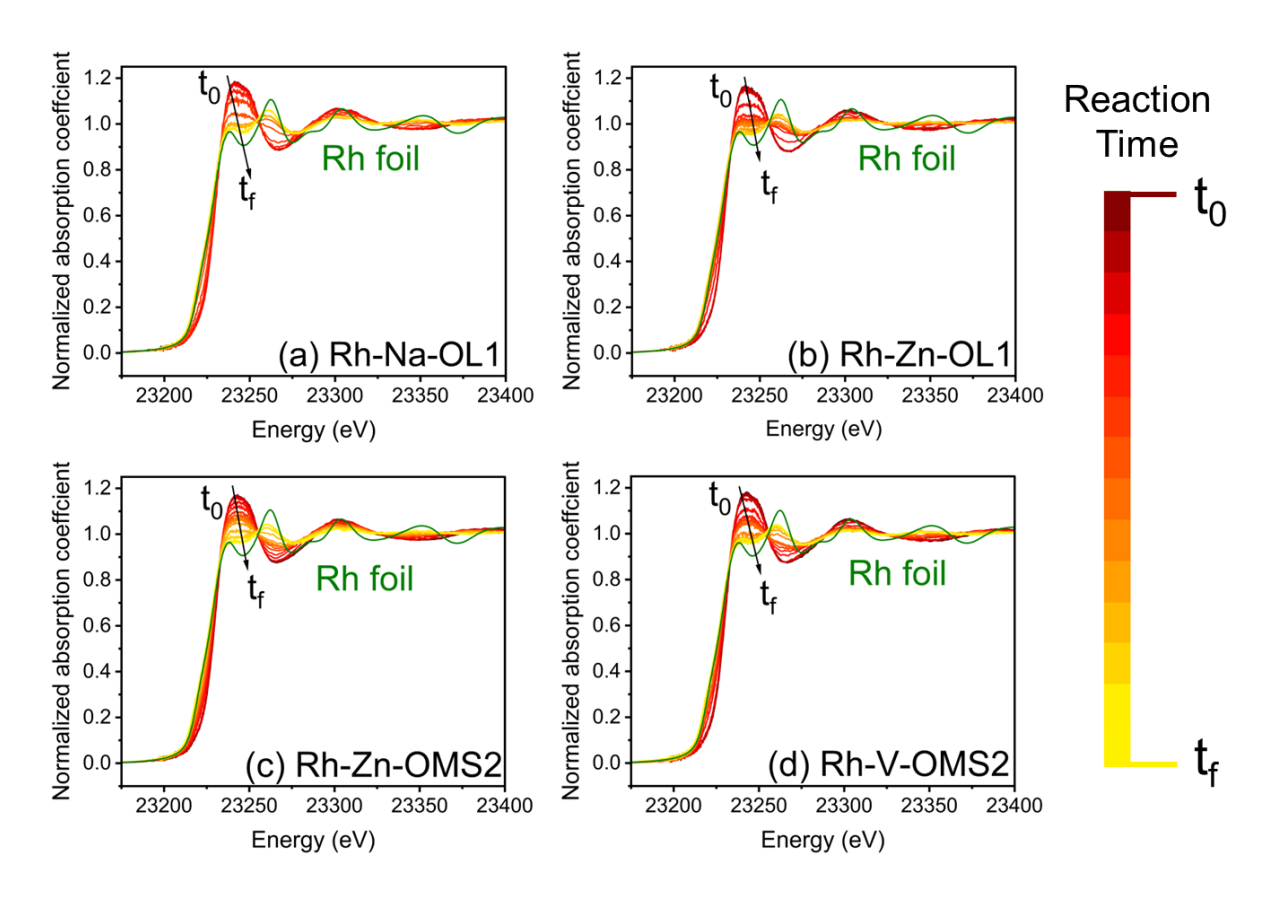


Figure 7. In situ XANES spectra at Rh K-edge for (a) Rh-Na-OL1, (b) Rh-Zn-OL1, (c) Rh-Zn-OMS2 and (d) Rh-V-OMS2 with to corresponding to 25°C and t<sub>final</sub>. XANES of Rh foil, Rh(0) standard, is shown in green.

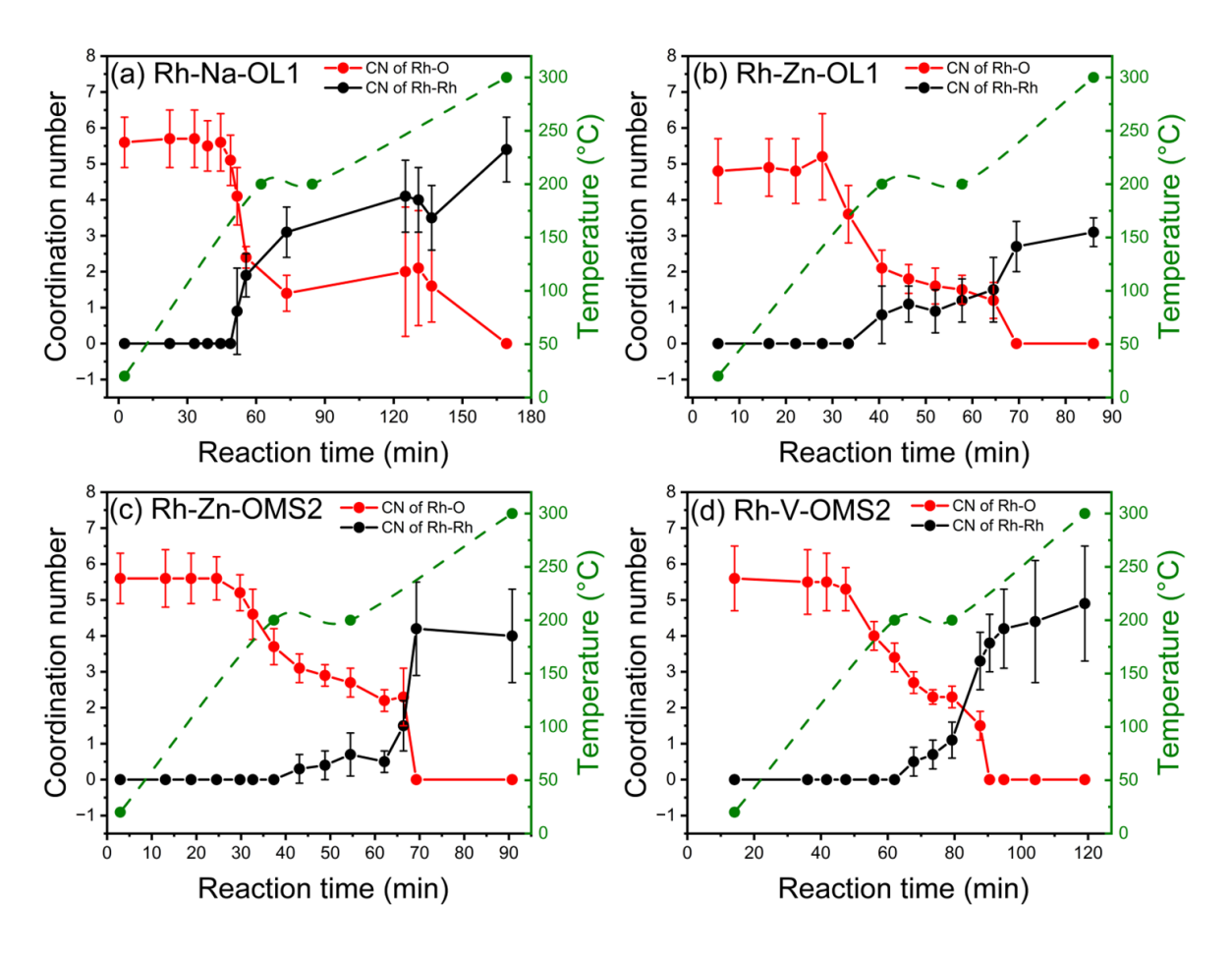


Figure 8. EXAFS fitting results for the coordination number of (a) Rh-Na-OL1, (b) Rh-Zn-OL1, (c) Rh-Zn-OMS2 and (d) Rh-V-OMS2 during the in situ CO<sub>2</sub> hydrogenation experiments.

Since the coordination numbers were obtained from EXAFS fitting and there is a positive correlation between the coordination number and the number of atoms in the cluster,[88] the number of atoms in the clusters in each sample can be calculated. Therefore, the coordination numbers from EXAFS fitting from the sample at 300°C for around 20 mins were used, and the number of atoms was calculated, as shown in Table. S7. The calculation is discussed in Note. S2. The mean interatomic distances (MIAD)[89, 90] of each sample were also calculated and shown in Table. S7 to represent the size of the clusters. The particle sizes calculated from the information

obtained from EXAFS fitting from the samples at 300°C for around 20 mins were mapped with the reaction rate of these four samples at 300°C reaction for around 20 mins. When the particle size is larger, the reaction rate is higher, as shown in Fig. S27, at the beginning of the reaction when the MnOx structure has not decomposed yet. This is in agreement with the literature, which found that for CO<sub>2</sub> hydrogenation, Rh clusters and small nanoparticles favored higher reaction rates than isolated single atoms.[91-93] More literature comparisons can be found in Table. S8 for CO<sub>2</sub> Hydrogenation.[92, 94-98] Our catalytic system of Rh-X-(OL1/OMS2) provides a potential innovative method to create clusters with low-nanoscale clusters from single Rh atoms. One of the advantages of the Rh-X-OMS materials is their inherent CO<sub>2</sub> sorption properties, which when coupled to their stable catalytic performance can lead to innovative combined capture and conversion catalysts, which is unique and novel to these materials.[99]

#### 3.8. CO<sub>2</sub> Hydrogenation DRIFTS

During CO<sub>2</sub> hydrogenation DRIFTS, both OL1 and OMS2 sample sets yield similar carbonyl surface species, between 2200-1800 cm<sup>-1</sup>, likely due to comparable interactions with MnO across OL1 and OMS2, shown in Fig. 9(a). The absence of the secondary bridge/hollow Rh-CO species on OL1 samples indicates a higher Rh dispersion on the surface of OL1 samples, which contributes to the dominance of linear CO on metallic Rh<sup>0</sup>. Based on Fig. 9(b), there is mainly formate (~1595 cm<sup>-1</sup>) dominant on Rh-Na-OL1. This bridged formate, as shown in Fig. S28 by the corresponding bridged formate C-H stretching at 2825 cm<sup>-1</sup>,[100] is likely the intermediate for methanation and is consistent with the main CH<sub>4</sub> selectivity from Rh-Na-OL1 shown in Fig. 2(c). Formate-mediated methanation is likely to occur through an initial rate-limited formation of HCOO\* surface species, then rapidly dissociates into CO\* and OH\*, which subsequently rapidly

forms CH<sub>4</sub> and H<sub>2</sub>O as the main products.[101] On the surface of Rh-Zn-OMS2, Rh-Zn-OL1, and Rh-V-OMS2, there are predominantly monodentate/bidentate carbonate species, which suggests the likelihood of a direct CO<sub>2</sub> dissociation pathway into CO which is not mediated by formate, consistent with the fact that methane formation is suppressed on this catalyst. In the C-H stretching region in Fig. S28, between 3000-2600 cm<sup>-1</sup>, we can observe the presence of gas phase methane over Rh-Na-OL1 and Rh-V-OMS2, showing they promote CH<sub>4</sub> formation. However, consistent with the lack of formate bands on all other catalysts, Rh-Na-OL1 is the only one which shows a corresponding C-H stretch associated with formate species, specifically bridged formate.[100, 102] The peaks found at 2760 and 2680 cm<sup>-1</sup> are attributed to the C-H stretching. In summary, the selectivity is consistent with the surface species we found during in situ CO<sub>2</sub> hydrogenation DRFITS, where the formation of methane was followed via the associative formate pathway, while the catalyst that favored CO via the RWGS showed no formate on the surface, likely indicating that formate was rapidly consumed and dissociated into CO and OH via the dissociative mechanism.

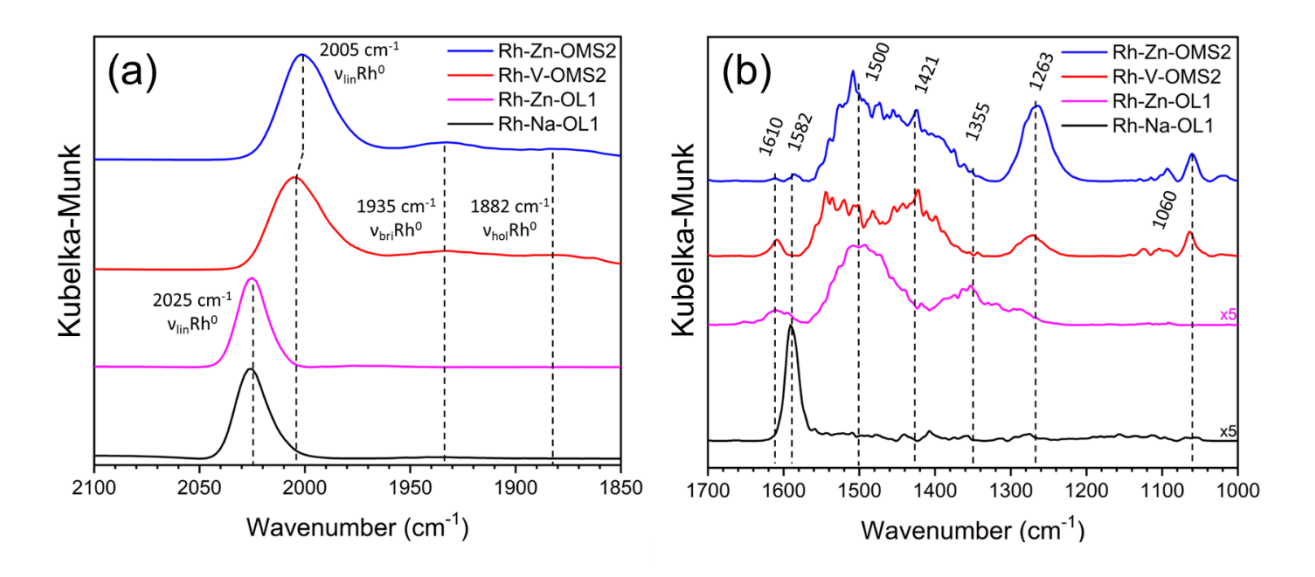


Figure 9. In situ CO<sub>2</sub> hydrogenation DRIFTS for Rh-X-MnOx showing the (a) Rh carbonyls region and (b) surface carbonates region. Conditions: 4:1:1 of H<sub>2</sub>: CO<sub>2</sub>: He feed gas, 300 °C, 1 atm, MCT detector, 4 cm<sup>-1</sup> resolution.

#### 4. Conclusions

We have evaluated multicomponent catalysts composed of Rh, different counterions, and MnO<sub>X</sub> frameworks for the CO<sub>2</sub> hydrogenation reaction. When different counterions were used, there were distinct differences in product selectivity based on the counterion species. Rh-V-OMS2 remained stable after 48 hrs, surpassing the net reactivity of other initially more active combinations. Compared with OMS2, while the OL1 structure can provide a more reducing environment with more CH<sub>4</sub> production and instantaneous high reactivity, OL1 structures did not have good stability for extended reaction times. The structure-function relationship in Rh-MnOxs was investigated, where the surface species attributed to both the methanation and RWGS pathway were identified via DRIFTS, and the structure was observed to be Rh clusters via in situ XAFS. The catalysts transitioned from Rh atoms with atomic dispersion after synthesis to small clusters and eventually nucleated into nanoparticles. We also found a positive correlation between the reaction rate and the particle size. Importantly, with detailed kinetic measurements and spectroscopic techniques, the addition of V not only stabilized the structure of the OMS2 host material but also sustained remarkable selectivity towards CO via the RWGS pathway for over 48 hrs. The nucleation of single-atom Rh into clusters indicates that the combination of single-atom Rh and MnOxs can provide us with Rh catalysis of low nanoscale or sub-nanoscale clusters, which has been proven more effective than single-atom catalysts and nanoparticles from previous publications.

## Acknowledge

This study is supported by the U.S. Department of Energy (DE-SC0012704). A.I.F. acknowledges the support of U.S. National Science Foundation under Award 2102299. This research used beamlines 7-BM (Quick X-ray Absorption and Scattering, QAS) and 8-ID (Inner-Shell Spectroscopy, ISS) of the National Synchrotron Light Source II, a Department of Energy (DOE) Office of Science User Facility operated by Brookhaven National Laboratory under Contract DE-SC0012704. Beamline operations were supported in part by the Synchrotron Catalysis Consortium (DOE Office of Basic Energy Sciences Grant DE-SC0012335). This research used STEM of the Center for Functional Nanomaterials (CFN), which is a U.S. Department of Energy Office of Science User Facility, at Brookhaven National Laboratory under Contract No. DE-SC0012704. J.D. Jimenez would like to acknowledge the BNL Goldhaber Distinguished Fellowship for support. We would like to thank E. Stavitski, S. Ehrlich, L. Ma, and N. Marinkovic for their help with XAFS data collection at the ISS and QAS beamline.

#### References

[1] J. Artz, T.E. Müller, K. Thenert, J. Kleinekorte, R. Meys, A. Sternberg, A. Bardow, W. Leitner, Sustainable conversion of carbon dioxide: an integrated review of catalysis and life cycle assessment, Chemical Reviews, 118 (2018) 434-504.

https://doi.org/10.1021/acs.chemrev.7b00435

- [2] K. Abbass, M.Z. Qasim, H. Song, M. Murshed, H. Mahmood, I. Younis, A review of the global climate change impacts, adaptation, and sustainable mitigation measures, Environmental Science and Pollution Research, 29 (2022) 42539-42559. <a href="https://doi.org/10.1007/s11356-022-19718-6">https://doi.org/10.1007/s11356-022-19718-6</a>
- [3] L. Al-Ghussain, Global warming: review on driving forces and mitigation, Environmental Progress & Sustainable Energy, 38 (2019) 13-21. <a href="https://doi.org/10.1002/ep.13041">https://doi.org/10.1002/ep.13041</a>
  [4] R. An, B. Yu, R. Li, Y.-M. Wei, Potential of energy savings and CO<sub>2</sub> emission reduction in China's iron and steel industry, Applied Energy, 226 (2018) 862-880.

https://doi.org/10.1016/j.apenergy.2018.06.044

[5] N. Muller, G. Herz, E. Reichelt, M. Jahn, CO<sub>2</sub> emission reduction potential in the steel industry by integration of a direct reduction process into existing steel mills, IAEA International Atomic Energy Agency, 49 (2018) 187-195.

http://inis.iaea.org/search/search.aspx?orig q=RN:49107596

[6] E.I. Koytsoumpa, C. Bergins, E. Kakaras, The CO<sub>2</sub> economy: review of CO<sub>2</sub> capture and reuse technologies, The Journal of Supercritical Fluids, 132 (2018) 3-16.

https://doi.org/10.1016/j.supflu.2017.07.029

[7] E.S. Rubin, J.E. Davison, H.J. Herzog, The cost of CO<sub>2</sub> capture and storage, International Journal of Greenhouse Gas Control, 40 (2015) 378-400.

https://doi.org/10.1016/j.ijggc.2015.05.018

[8] R. Steeneveldt, B. Berger, T.A. Torp, CO<sub>2</sub> capture and storage: closing the knowing–doing gap, Chemical Engineering Research and Design, 84 (2006) 739-763. https://doi.org/10.1205/cherd05049

[9] M.N. Anwar, A. Fayyaz, N.F. Sohail, M.F. Khokhar, M. Baqar, W.D. Khan, K. Rasool, M. Rehan, A.S. Nizami, CO<sub>2</sub> capture and storage: A way forward for sustainable environment, Journal of Environmental Management, 226 (2018) 131-144.

https://doi.org/10.1016/j.jenvman.2018.08.009

- [10] E.S. Sanz-Pérez, C.R. Murdock, S.A. Didas, C.W. Jones, Direct capture of CO<sub>2</sub> from ambient air, Chemical Reviews, 116 (2016) 11840-11876. <a href="https://doi.org/10.1021/acs.chemrev.6b00173">https://doi.org/10.1021/acs.chemrev.6b00173</a>
  [11] C.H. Huang, C.S. Tan, A review: CO<sub>2</sub> utilization, Aerosol and Air Quality Research, 14
- [11] C.-H. Huang, C.-S. Tan, A review: CO<sub>2</sub> utilization, Aerosol and Air Quality Research, 14 (2014) 480-499. <a href="https://doi.org/10.4209/aaqr.2013.10.0326">https://doi.org/10.4209/aaqr.2013.10.0326</a>
- [12] B. Li, Y. Duan, D. Luebke, B. Morreale, Advances in CO<sub>2</sub> capture technology: A patent review, Applied Energy, 102 (2013) 1439-1447. https://doi.org/10.1016/j.apenergy.2012.09.009
- [13] X. Han, T. Mou, S. Liu, M. Ji, Q. Gao, Q. He, H. Xin, H. Zhu, Heterostructured  $Bi-Cu_2S$  nanocrystals for efficient  $CO_2$  electroreduction to formate, Nanoscale Horizons, 7 (2022) 508-514. https://doi.org/10.1039/D1NH00661D
- [14] N.H. Khdary, A.S. Alayyar, L.M. Alsarhan, S. Alshihri, M. Mokhtar, Metal oxides as catalyst/supporter for CO<sub>2</sub> capture and conversion, review, Catalysts, 12 (2022) 300. https://doi.org/10.3390/catal12030300
- [15] S. Zhang, Z. Wu, X. Liu, K. Hua, Z. Shao, B. Wei, C. Huang, H. Wang, Y. Sun, A short review of recent advances in direct CO<sub>2</sub> hydrogenation to alcohols, Topics in Catalysis, 64 (2021) 371-394. <a href="https://doi.org/10.1007/s11244-020-01405-w">https://doi.org/10.1007/s11244-020-01405-w</a>
- [16] C. Song, Global challenges and strategies for control, conversion and utilization of CO<sub>2</sub> for sustainable development involving energy, catalysis, adsorption and chemical processing, Catalysis Today, 115 (2006) 2-32. <a href="https://doi.org/10.1016/j.cattod.2006.02.029">https://doi.org/10.1016/j.cattod.2006.02.029</a>
- [17] T. Mou, H.S. Pillai, S. Wang, M. Wan, X. Han, N.M. Schweitzer, F. Che, H. Xin, Bridging the complexity gap in computational heterogeneous catalysis with machine learning, Nature Catalysis, 6 (2023) 122-136. https://doi.org/10.1038/s41929-023-00911-w
- [18] S. Kanuri, S. Roy, C. Chakraborty, S.P. Datta, S.A. Singh, S. Dinda, An insight of CO<sub>2</sub> hydrogenation to methanol synthesis: Thermodynamics, catalysts, operating parameters, and reaction mechanism, Int J Energy Res., 46 (2022) 5503-5522. https://doi.org/10.1002/er.7562
- [19] R.-P. Ye, J. Ding, W. Gong, M.D. Argyle, Q. Zhong, Y. Wang, C.K. Russell, Z. Xu, A.G. Russell, Q. Li, M. Fan, Y.-G. Yao, CO<sub>2</sub> hydrogenation to high-value products via heterogeneous catalysis, Nature Communications, 10 (2019) 5698. <a href="https://doi.org/10.1038/s41467-019-13638-9">https://doi.org/10.1038/s41467-019-13638-9</a>

- [20] W.-H. Wang, Y. Himeda, J.T. Muckerman, G.F. Manbeck, E. Fujita, CO<sub>2</sub> hydrogenation to formate and methanol as an alternative to photo- and electrochemical CO<sub>2</sub> reduction, Chemical Reviews, 115 (2015) 12936-12973. https://doi.org/10.1021/acs.chemrev.5b00197
- [21] S. Saeidi, N.A.S. Amin, M.R. Rahimpour, Hydrogenation of CO<sub>2</sub> to value-added products—A review and potential future developments, Journal of CO<sub>2</sub> Utilization, 5 (2014) 66-81. https://doi.org/10.1016/j.jcou.2013.12.005
- [22] S.S. Ali, S.S. Ali, N. Tabassum, A review on CO<sub>2</sub> hydrogenation to ethanol: Reaction mechanism and experimental studies, Journal of Environmental Chemical Engineering, 10 (2022) 106962. https://doi.org/10.1016/j.jece.2021.106962
- [23] X. Zhu, Y. Li, Review of two-dimensional materials for electrochemical CO<sub>2</sub> reduction from a theoretical perspective, Wiley Interdisciplinary Reviews: Computational Molecular Science, 9 (2019) e1416. https://doi.org/10.1002/wcms.1416
- [24] V. Giulimondi, S.K. Kaiser, M. Agrachev, F. Krumeich, A.H. Clark, S. Mitchell, G. Jeschke, J. Pérez-Ramírez, Redispersion strategy for high-loading carbon-supported metal catalysts with controlled nuclearity, Journal of Materials Chemistry A, 10 (2022) 5953-5961. https://doi.org/10.1039/D1TA09238C
- [25] L. Wang, S. Deo, K. Dooley, M.J. Janik, R.M. Rioux, Influence of metal nuclearity and physicochemical properties of ceria on the oxidation of carbon monoxide, Chinese Journal of Catalysis, 41 (2020) 951-962. <a href="https://doi.org/10.1016/S1872-2067(20)63557-4">https://doi.org/10.1016/S1872-2067(20)63557-4</a>
- [26] T. Giovenzana, M. Guidotti, E. Lucenti, A. Orbelli Biroli, L. Sordelli, A. Sironi, R. Ugo, Synthesis and catalytic activity of titanium silsesquioxane frameworks as models of titanium active surface sites of controlled nuclearity, Organometallics, 29 (2010) 6687-6694. https://doi.org/10.1021/om100636h
- [27] X. Li, X. Yang, Y. Huang, T. Zhang, B. Liu, Supported noble-metal single atoms for heterogeneous catalysis, Advanced Materials, 31 (2019) 1902031.

https://doi.org/10.1002/adma.201902031

- [28] M. Li, H. Wang, W. Luo, P.C. Sherrell, J. Chen, J. Yang, Heterogeneous single-atom catalysts for electrochemical CO<sub>2</sub> reduction reaction, Advanced Materials, 32 (2020) 2001848. https://doi.org/10.1002/adma.202001848
- [29] Q. Wang, C. Cai, M. Dai, J. Fu, X. Zhang, H. Li, H. Zhang, K. Chen, Y. Lin, H. Li, J. Hu, M. Miyauchi, M. Liu, Recent advances in strategies for improving the performance of CO<sub>2</sub> reduction reaction on single atom catalysts, Small Science, 1 (2021) 2000028.

https://doi.org/10.1002/smsc.202000028

- [30] P. Panagiotopoulou, Hydrogenation of CO<sub>2</sub> over supported noble metal catalysts, Applied Catalysis A: General, 542 (2017) 63-70. <a href="https://doi.org/10.1016/j.apcata.2017.05.026">https://doi.org/10.1016/j.apcata.2017.05.026</a>
- [31] Y. Han, H. Xu, Y. Su, Z.-l. Xu, K. Wang, W. Wang, Noble metal (Pt, Au@Pd) nanoparticles supported on metal organic framework (MOF-74) nanoshuttles as high-selectivity CO<sub>2</sub> conversion catalysts, Journal of Catalysis, 370 (2019) 70-78.

https://doi.org/10.1016/j.jcat.2018.12.005

- [32] Y. Yang, J. Liu, F. Liu, D. Wu, Reaction mechanism of CO<sub>2</sub> methanation over Rh/TiO<sub>2</sub> catalyst, Fuel, 276 (2020) 118093. <a href="https://doi.org/10.1016/j.fuel.2020.118093">https://doi.org/10.1016/j.fuel.2020.118093</a>
- [33] M.R. Gogate, R.J. Davis, Comparative study of CO and  $CO_2$  hydrogenation over supported Rh–Fe catalysts, Catalysis Communications, 11 (2010) 901-906.

https://doi.org/10.1016/j.catcom.2010.03.020

[34] A. Karelovic, P. Ruiz,  $CO_2$  hydrogenation at low temperature over  $Rh/\gamma$ - $Al_2O_3$  catalysts: Effect of the metal particle size on catalytic performances and reaction mechanism, Applied Catalysis B: Environmental, 113-114 (2012) 237-249.

https://doi.org/10.1016/j.apcatb.2011.11.043

- [35] J. Kim, H. Ha, W.H. Doh, K. Ueda, K. Mase, H. Kondoh, B.S. Mun, H.Y. Kim, J.Y. Park, How Rh surface breaks CO<sub>2</sub> molecules under ambient pressure, Nature Communications, 11 (2020) 5649. https://doi.org/10.1038/s41467-020-19398-1
- [36] H. Xiong, A.K. Datye, Y. Wang, Thermally stable single-atom heterogeneous catalysts, Advanced Materials, 33 (2021) 2004319. https://doi.org/10.1002/adma.202004319
- [37] H. Lv, W. Guo, M. Chen, H. Zhou, Y. Wu, Rational construction of thermally stable single atom catalysts: From atomic structure to practical applications, Chinese Journal of Catalysis, 43 (2022) 71-91. <a href="https://doi.org/10.1016/S1872-2067(21)63888-3">https://doi.org/10.1016/S1872-2067(21)63888-3</a>
- [38] L. Xu, D. Liu, D. Chen, H. Liu, J. Yang, Size and shape controlled synthesis of rhodium nanoparticles, Heliyon, 5 (2019) e01165. <a href="https://doi.org/10.1016/j.heliyon.2019.e01165">https://doi.org/10.1016/j.heliyon.2019.e01165</a>
- [39] A. Cervantes Uribe, G.A. Del Angel Montes, G. Torres-Torres, A. Vázquez-Zavala, F. González-García, A. Cordero-García, R. Ojeda-López, Correlation of Rh particle size with CO chemisorption: Effect on the catalytic oxidation of MTBE, Journal of Composites Science, 2019. https://doi.org/10.3390/jcs3030081
- [40] S. Xie, X.Y. Liu, Y. Xia, Shape-controlled syntheses of rhodium nanocrystals for the enhancement of their catalytic properties, Nano Research, 8 (2015) 82-96.

https://doi.org/10.1007/s12274-014-0674-x

[41] M. Ojeda, S. Rojas, M. Boutonnet, F.J. Pérez-Alonso, F. Javier García-García, J.L.G. Fierro, Synthesis of Rh nano-particles by the microemulsion technology: Particle size effect on the CO+H<sub>2</sub> reaction, Applied Catalysis A: General, 274 (2004) 33-41.

https://doi.org/10.1016/j.apcata.2004.05.014

[42] S.L. Brock, N. Duan, Z.R. Tian, O. Giraldo, H. Zhou, S.L. Suib, A review of porous manganese oxide materials, Chemistry of Materials, 10 (1998) 2619-2628.

https://doi.org/10.1021/cm980227h

- [43] W.N. Li, J. Yuan, X.F. Shen, S. Gomez-Mower, L.P. Xu, S. Sithambaram, M. Aindow, S.L. Suib, Hydrothermal synthesis of structure- and shape-controlled manganese oxide octahedral molecular sieve nanomaterials, Advanced Functional Materials, 16 (2006) 1247-1253. https://doi.org/10.1002/adfm.200500504
- [44] N.D. Wasalathanthri, A.S. Poyraz, S. Biswas, Y. Meng, C.-H. Kuo, D.A. Kriz, S.L. Suib, High-performance catalytic CH<sub>4</sub> oxidation at low temperatures: Inverse micelle synthesis of amorphous mesoporous manganese oxides and mild transformation to  $K_2$ –xMn<sub>8</sub>O<sub>16</sub> and  $\epsilon$ -MnO<sub>2</sub>, The Journal of Physical Chemistry C, 119 (2015) 1473-1482.

https://doi.org/10.1021/jp5108558

- [45] X. Chen, Y.-F. Shen, S.L. Suib, C.L. O'Young, Catalytic decomposition of 2-propanol over different metal-cation-doped OMS-2 materials, Journal of Catalysis, 197 (2001) 292-302. https://doi.org/10.1006/jcat.2000.3063
- [46] L. Tabassum, H. Tasnim, A.G. Meguerdichian, W.S. Willis, J. Macharia, C. Price, Y. Dang, S.L. Suib, Enhanced catalytic activity of a vanadium-doped mesoporous octahedral molecular sieve-2 (K-OMS-2) toward hydrogen evolution reaction, ACS Applied Energy Materials, 3 (2020) 12185-12193. https://doi.org/10.1021/acsaem.0c02245

- [47] R. Dalebout, L. Barberis, N.L. Visser, J.E.S. van der Hoeven, A.M.J. van der Eerden, J.A. Stewart, F. Meirer, K.P. de Jong, P.E. de Jongh, Manganese oxide as a promoter for copper catalysts in CO<sub>2</sub> and CO hydrogenation, ChemCatChem, 14 (2022) e202200451. https://doi.org/10.1002/cctc.202200451
- [48] K. Zhao, Z. Li, L. Bian,  $CO_2$  methanation and co-methanation of CO and  $CO_2$  over Mn-promoted Ni/Al<sub>2</sub>O<sub>3</sub> catalysts, Frontiers of Chemical Science and Engineering, 10 (2016) 273-280. https://doi.org/10.1007/s11705-016-1563-5
- [49] A. Iyer, J. Del-Pilar, C.K. King'ondu, E. Kissel, H.F. Garces, H. Huang, A.M. El-Sawy, P.K. Dutta, S.L. Suib, Water oxidation catalysis using amorphous manganese oxides, octahedral molecular sieves (OMS-2), and octahedral layered (OL-1) manganese oxide structures, The Journal of Physical Chemistry C, 116 (2012) 6474-6483. https://doi.org/10.1021/jp2120737
- [50] L.J. Garces, J.A. Galeano, H.F. Garces, S.L. Suib, B. Hincapie, Oxidation of cyclopentene with manganese oxides octahedral molecular sieves with layer and tunnel structures, ChemistrySelect, 7 (2022) e202104110. https://doi.org/10.1002/slct.202104110
- [51] C.K. King'ondu, N. Opembe, C.-h. Chen, K. Ngala, H. Huang, A. Iyer, H.F. Garcés, S.L. Suib, Manganese Oxide Octahedral Molecular Sieves (OMS-2) Multiple Framework Substitutions: A New Route to OMS-2 Particle Size and Morphology Control, Advanced Functional Materials, 21 (2011) 312-323. https://doi.org/10.1002/adfm.201001020
- [52] K. Świrk Da Costa, P. Summa, D. Wierzbicki, M. Motak, P. Da Costa, Vanadium promoted Ni(Mg,Al)O hydrotalcite-derived catalysts for CO<sub>2</sub> methanation, International Journal of Hydrogen Energy, 46 (2021) 17776-17783. https://doi.org/10.1016/j.ijhydene.2021.02.172
- [53] H.C. Genuino, Y. Meng, D.T. Horvath, C.-H. Kuo, M.S. Seraji, A.M. Morey, R.L. Joesten, S.L. Suib, Enhancement of catalytic activities of octahedral molecular sieve manganese oxide for total and preferential CO oxidation through vanadium ion framework substitution,

ChemCatChem, 5 (2013) 2306-2317. https://doi.org/10.1002/cctc.201300005

[54] T.A. Le, T.W. Kim, S.H. Lee, E.D. Park, Effects of Na content in Na/Ni/SiO<sub>2</sub> and Na/Ni/CeO<sub>2</sub> catalysts for CO and CO<sub>2</sub> methanation, Catalysis Today, 303 (2018) 159-167.

https://doi.org/10.1016/j.cattod.2017.09.031

- [55] Y. Xu, P. Zhai, Y. Deng, J. Xie, X. Liu, S. Wang, D. Ma, Highly selective olefin production from  $CO_2$  hydrogenation on iron catalysts: A subtle synergy between manganese and sodium additives, Angewandte Chemie International Edition, 59 (2020) 21736-21744.
- https://doi.org/10.1002/anie.202009620
- [56] Y. Zheng, C. Xu, X. Zhang, Q. Wu, J. Liu, Synergistic effect of alkali Na and K promoter on Fe-Co-Cu-Al catalysts for CO<sub>2</sub> hydrogenation to light hydrocarbons, Catalysts, 11 (2021) 735. https://doi.org/10.3390/catal11060735
- [57] X.F. Shen, Y.S. Ding, J. Liu, J. Cai, K. Laubernds, R.P. Zerger, A. Vasiliev, M. Aindow, S.L. Suib, Control of nanometer-scale tunnel sizes of porous manganese oxide octahedral molecular sieve nanomaterials, Advanced Materials, 17 (2005) 805-809.

https://doi.org/10.1002/adma.200401225

[58] N.P. Arias, M.E. Becerra, O. Giraldo, Structural and electrical studies for birnessite-type materials synthesized by solid-state reactions, Nanomaterials, 9 (2019) 1156. https://doi.org/10.3390/nano9081156

- [59] M.T. Martinez, A.S. Lima, N. Bocchi, M.F.S. Teixeira, Voltammetric performance and application of a sensor for sodium ions constructed with layered birnessite-type manganese oxide, Talanta, 80 (2009) 519-525. <a href="https://doi.org/10.1016/j.talanta.2009.07.015">https://doi.org/10.1016/j.talanta.2009.07.015</a>
- [60] M. Fedyna, P. Legutko, J. Gryboś, J. Janas, X. Yu, Z. Zhao, A. Kotarba, Z. Sojka, Screening investigations into the effect of cryptomelane doping with 3d transition metal cations on the catalytic activity in soot oxidation, NO<sub>2</sub> formation and SO<sub>2</sub> resistance, Applied Catalysis A: General, 624 (2021) 118302. https://doi.org/10.1016/j.apcata.2021.118302
- [61] S. Ching, E.J. Welch, S.M. Hughes, A.B.F. Bahadoor, S.L. Suib, Nonaqueous sol–gel syntheses of microporous manganese oxides, Chemistry of Materials, 14 (2002) 1292-1299. https://doi.org/10.1021/cm010780q
- [62] M. Sun, B. Zhang, H. Liu, B. He, F. Ye, L. Yu, C. Sun, H. Wen, The effect of acid/alkali treatment on the catalytic combustion activity of manganese oxide octahedral molecular sieves, RSC Advances, 7 (2017) 3958-3965. https://doi.org/10.1039/C6RA27700D
- [63] S. Kattel, P. Liu, J.G. Chen, Tuning selectivity of CO<sub>2</sub> hydrogenation reactions at the metal/oxide interface, Journal of the American Chemical Society, 139 (2017) 9739-9754. https://doi.org/10.1021/jacs.7b05362
- [64] M.K. Gnanamani, G. Jacobs, R.A. Keogh, W.D. Shafer, D.E. Sparks, S.D. Hopps, G.A. Thomas, B.H. Davis, Fischer-Tropsch synthesis: Effect of pretreatment conditions of cobalt on activity and selectivity for hydrogenation of carbon dioxide, Applied Catalysis A: General, 499 (2015) 39-46. <a href="https://doi.org/10.1016/j.apcata.2015.03.046">https://doi.org/10.1016/j.apcata.2015.03.046</a>
- [65] M.E. Dry, T. Shingles, C.S. van H. Botha, Factors influencing the formation of carbon on iron Fischer-Tropsch catalysts: I. The influence of promoters, Journal of Catalysis, 17 (1970) 341-346. <a href="https://doi.org/10.1016/0021-9517(70)90109-0">https://doi.org/10.1016/0021-9517(70)90109-0</a>
- [66] R.L. Oliveira, I.G. Bitencourt, F.B. Passos, Partial oxidation of methane to syngas on  $Rh/Al_2O_3$  and  $Rh/Ce-ZrO_2$  catalysts, Journal of the Brazilian Chemical Society 24 (2013) 68-75. <u>https://doi.org/10.1590/S0103-50532013000100010</u>
- [67] J.A. Wang, T. López, X. Bokhimi, O. Novaro, Phase composition, reducibility and catalytic activity of Rh/zirconia and Rh/zirconia-ceria catalysts, Journal of Molecular Catalysis A: Chemical, 239 (2005) 249-256. https://doi.org/10.1016/j.molcata.2005.06.021
- [68] P. Fornasiero, R. Dimonte, G.R. Rao, J. Kaspar, S. Meriani, A. Trovarelli, M. Graziani, Rhloaded CeO<sub>2</sub>-ZrO<sub>2</sub> solid-solutions as highly efficient oxygen exchangers: Dependence of the reduction behavior and the oxygen storage capacity on the structural-properties, Journal of Catalysis, 151 (1995) 168-177. https://doi.org/10.1006/jcat.1995.1019
- [69] V. Rico-Pérez, A.J.A.S. Bueno-López, Effect of RhOx/CeO<sub>2</sub> calcination on metal-support interaction and catalytic activity for N<sub>2</sub>O decomposition, Applied Sciences, 4 (2014) 468-481. https://doi.org/10.3390/app4030468
- [70] Q. Zheng, R. Farrauto, M. Deeba, I. Valsamakis, Part I: A comparative thermal aging study on the regenerability of Rh/Al<sub>2</sub>O<sub>3</sub> and Rh/CexOy-ZrO<sub>2</sub> as model catalysts for automotive three way catalysts, Catalysts, 5 (2015) 1770-1796. <a href="https://doi.org/10.3390/catal5041770">https://doi.org/10.3390/catal5041770</a>
- [71] M. Wang, L. Zhang, W. Huang, Y. Zhou, H. Zhao, J. Lv, J. Tian, X. Kan, J. Shi, Pt/MnO<sub>2</sub> nanosheets: facile synthesis and highly efficient catalyst for ethylene oxidation at low temperature, RSC Advances, 7 (2017) 14809-14815. <a href="https://doi.org/10.1039/C6RA26529D">https://doi.org/10.1039/C6RA26529D</a>

- [72] N. Dong, J. Fu, Q. Ye, M. Chen, Z. Fu, H. Dai, Effect of preparation method on catalytic performance of Ag/OMS-2 for the oxidation of ethyl acetate and formaldehyde, Catalysis Surveys from Asia, 24 (2020) 259-268. <a href="https://doi.org/10.1007/s10563-020-09311-7">https://doi.org/10.1007/s10563-020-09311-7</a> [73] S. Philipp, A. Drochner, J. Kunert, H. Vogel, J. Theis, E.S. Lox, Investigation of NO adsorption
- and NO/O<sub>2</sub> co-adsorption on NOx-storage-components by DRIFT-spectroscopy, Topics in Catalysis, 30 (2004) 235-238. <a href="https://doi.org/10.1023/B:TOCA.0000029755.35282.00">https://doi.org/10.1023/B:TOCA.0000029755.35282.00</a>
- [74] J.A. Lercher, A. Jentys, Chapter 13 Infrared and Raman Spectroscopy for Characterizing Zeolites, in: J. Čejka, H. van Bekkum, A. Corma, F. Schüth (Eds.) Studies in Surface Science and Catalysis, Elsevier2007, pp. 435-476.
- [75] A. Zecchina, D. Scarano, S. Bordiga, G. Spoto, C. Lamberti, Surface structures of oxides and halides and their relationships to catalytic properties, Advances in Catalysis, 46 (2001) 265-397. https://doi.org/10.1016/S0360-0564(02)46024-5
- [76] H. Zhu, Y. Li, X. Zheng, In-situ DRIFTS study of CeO<sub>2</sub> supported Rh catalysts for N<sub>2</sub>O decomposition, Applied Catalysis A: General, 571 (2019) 89-95. https://doi.org/10.1016/j.apcata.2018.12.020
- [77] I.A. Pankin, A. Martini, K.A. Lomachenko, A.V. Soldatov, S. Bordiga, E. Borfecchia, Identifying Cu-oxo species in Cu-zeolites by XAS: A theoretical survey by DFT-assisted XANES simulation and EXAFS wavelet transform, Catalysis Today, 345 (2020) 125-135. https://doi.org/10.1016/j.cattod.2019.09.032
- [78] J. Timoshenko, A. Kuzmin, Wavelet data analysis of EXAFS spectra, Computer Physics Communications, 180 (2009) 920-925. <a href="https://doi.org/10.1016/j.cpc.2008.12.020">https://doi.org/10.1016/j.cpc.2008.12.020</a>
- [79] T.J. Penfold, I. Tavernelli, C.J. Milne, M. Reinhard, A.E. Nahhas, R. Abela, U. Rothlisberger, M. Chergui, A wavelet analysis for the X-ray absorption spectra of molecules, The Journal of Chemical Physics, 138 (2013) 014104. https://doi.org/10.1063/1.4772766
- [80] L.R. Pahalagedara, S. Dharmarathna, C.K. King'ondu, M.N. Pahalagedara, Y.T. Meng, C.H. Kuo, S.L. Suib, Microwave-assisted hydrothermal synthesis of  $\alpha$ -MnO<sub>2</sub>: Lattice expansion via rapid temperature ramping and framework substitution, The Journal of Physical Chemistry C, 118 (2014) 20363-20373. https://doi.org/10.1021/jp505306q
- [81] R. Hu, C. Yan, L. Xie, Y. Cheng, D. Wang, Selective oxidation of CO in rich hydrogen stream over Ag/OMS-2 catalyst, International Journal of Hydrogen Energy, 36 (2011) 64-71. https://doi.org/10.1016/j.ijhydene.2010.09.047
- [82] J. Chen, X. Tang, J. Liu, E. Zhan, J. Li, X. Huang, W. Shen, Synthesis and characterization of Ag-hollandite nanofibers and its catalytic application in ethanol oxidation, Chemistry of Materials, 19 (2007) 4292-4299. https://doi.org/10.1021/cm070904k
- [83] J. Wang, S. Chen, R. Qin, R. Wang, L. Yu, L. Chen, Infinitesimal Pt species greatly enhance polyvalent OMS-2 for the efficient catalytic combustion of toluene, Chemical Physics Letters, 806 (2022) 140028. https://doi.org/10.1016/j.cplett.2022.140028
- [84] A. Khorshidi, M. Panahdar, R. Badihi, Ru-modified octahedral manganese oxide molecular sieve (Ru-OMS-2) as a reusable heterogeneous catalyst in selective oxidation of olanzapine and other polycyclic compounds, Catalysis Letters, (2024). <a href="https://doi.org/10.1007/s10562-023-04557-y">https://doi.org/10.1007/s10562-023-04557-y</a>
- [85] P. Chaurand, J. Rose, V. Briois, M. Salome, O. Proux, V. Nassif, L. Olivi, J. Susini, J.-L. Hazemann, J.-Y. Bottero, New methodological approach for the vanadium K-edge X-ray absorption near-edge structure interpretation: Application to the speciation of vanadium in

- oxide phases from steel slag, The Journal of Physical Chemistry B, 111 (2007) 5101-5110. https://doi.org/10.1021/jp063186i
- [86] J. Li, Y. Li, P.K. Routh, E. Makagon, I. Lubomirsky, A.I. Frenkel, Comparative analysis of XANES and EXAFS for local structural characterization of disordered metal oxides, Journal of Synchrotron Radiation, 28 (2021) 1511-1517. <a href="https://doi.org/10.1107/S1600577521007025">https://doi.org/10.1107/S1600577521007025</a>
  [87] A. Frenkel, Solving the 3D structure of metal nanoparticles, Zeitschrift für Kristallographie Crystalline Materials, 222 (2007) 605-611. <a href="https://doi.org/10.1524/zkri.2007.222.11.605">https://doi.org/10.1524/zkri.2007.222.11.605</a>
  [88] D. Glasner, A.I. Frenkel, Geometrical characteristics of regular polyhedra: Application to EXAFS studies of nanoclusters, AIP Conference Proceedings, 882 (2007) 746-748. <a href="https://doi.org/10.1063/1.2644651">https://doi.org/10.1063/1.2644651</a>
- [89] L.-L. Wang, D.D. Johnson, Shear instabilities in metallic nanoparticles: Hydrogen-stabilized structure of Pt37 on carbon, Journal of the American Chemical Society, 129 (2007) 3658-3664. https://doi.org/10.1021/ja068750h
- [90] L.L. Wang, D.D. Johnson, Density functional study of structural trends for late-transition-metal 13-atom clusters, Physical Review B, 75 (2007) 235405. https://doi.org/10.1103/PhysRevB.75.235405
- [91] J.C. Matsubu, V.N. Yang, P. Christopher, Isolated metal active site concentration and stability control catalytic CO<sub>2</sub> reduction selectivity, Journal of the American Chemical Society, 137 (2015) 3076-3084. https://doi.org/10.1021/ja5128133
- [92] J.C. Matsubu, S. Zhang, L. DeRita, N.S. Marinkovic, J.G. Chen, G.W. Graham, X. Pan, P. Christopher, Adsorbate-mediated strong metal—support interactions in oxide-supported Rh catalysts, Nature Chemistry, 9 (2017) 120-127. <a href="https://doi.org/10.1038/nchem.2607">https://doi.org/10.1038/nchem.2607</a>
  [93] Y. Zheng, Q. Wang, Q. Yang, S. Wang, M.J. Hülsey, S. Ding, S. Furukawa, M. Li, N. Yan, X. Ma, Boosting the hydroformylation activity of a Rh/CeO<sub>2</sub> single-atom catalyst by tuning surface deficiencies, ACS Catalysis, 13 (2023) 7243-7255. <a href="https://doi.org/10.1021/acscatal.3c00810">https://doi.org/10.1021/acscatal.3c00810</a>
  [94] D. Heyl, U. Rodemerck, U. Bentrup, Mechanistic study of low-temperature CO<sub>2</sub> hydrogenation over modified Rh/Al<sub>2</sub>O<sub>3</sub> catalysts, ACS Catalysis, 6 (2016) 6275-6284. <a href="https://doi.org/10.1021/acscatal.6b01295">https://doi.org/10.1021/acscatal.6b01295</a>
- [95] M. Danielis, J.D. Jiménez, N. Rui, J. Moncada, L.E. Betancourt, A. Trovarelli, J.A. Rodriguez, S.D. Senanayake, S. Colussi, Tuning the hydrogenation of CO₂ to CH₄ over mechano-chemically prepared palladium supported on ceria, Applied Catalysis A: General, 660 (2023) 119185. https://doi.org/10.1016/j.apcata.2023.119185
- [96] T. Sakpal, L. Lefferts, Structure-dependent activity of CeO<sub>2</sub> supported Ru catalysts for CO<sub>2</sub> methanation, Journal of Catalysis, 367 (2018) 171-180. https://doi.org/10.1016/j.jcat.2018.08.027
- [97] I.C.t. Have, J.J.G. Kromwijk, M. Monai, D. Ferri, E.B. Sterk, F. Meirer, B.M. Weckhuysen, Uncovering the reaction mechanism behind CoO as active phase for CO<sub>2</sub> hydrogenation, Nature Communications, 13 (2022) 324. <a href="https://doi.org/10.1038/s41467-022-27981-x">https://doi.org/10.1038/s41467-022-27981-x</a> [98] S. Li, Y. Xu, H. Wang, B. Teng, Q. Liu, Q. Li, L. Xu, X. Liu, J. Lu, Tuning the CO<sub>2</sub> hydrogenation
- selectivity of rhodium single-atom catalysts on zirconium dioxide with alkali ions, Angewandte Chemie International Edition, 62 (2023) e202218167. <a href="https://doi.org/10.1002/anie.202218167">https://doi.org/10.1002/anie.202218167</a> [99] L. Espinal, W. Wong-Ng, J.A. Kaduk, A.J. Allen, C.R. Snyder, C. Chiu, D.W. Siderius, L. Li, E. Cockayne, A.E. Espinal, S.L. Suib, Time-dependent CO<sub>2</sub> sorption hysteresis in a one-dimensional

microporous octahedral molecular sieve, Journal of the American Chemical Society, 134 (2012) 7944-7951. https://doi.org/10.1021/ja3014133

[100] C. Li, Y. Sakata, T. Arai, K. Domen, K.-i. Maruya, T. Onishi, Adsorption of carbon monoxide and carbon dioxide on cerium oxide studied by Fourier-transform infrared spectroscopy. Part 2.—Formation of formate species on partially reduced CeO<sub>2</sub> at room temperature, Journal of the Chemical Society, Faraday Transactions 1: Physical Chemistry in Condensed Phases, 85 (1989) 1451-1461. <a href="https://doi.org/10.1039/F19898501451">https://doi.org/10.1039/F19898501451</a>

[101] Y. Song, H. Wu, Y. Liu, G. Chen, R. Jia, L. Shi, Z. Shen, G. Li, J.H. Bitter, X. Wang, L. Huang, Oxygen vacancy regulated valence states of Pt on rutile TiO<sub>2</sub> promote catalytic oxidation of HCHO, Applied Catalysis A: General, 660 (2023) 119186.

https://doi.org/10.1016/j.apcata.2023.119186

[102] Y. Guo, S. Mei, K. Yuan, D.-J. Wang, H.-C. Liu, C.-H. Yan, Y.-W. Zhang, Low-temperature CO<sub>2</sub> methanation over CeO<sub>2</sub>-supported Ru single atoms, nanoclusters, and nanoparticles competitively tuned by strong metal—support interactions and H-spillover effect, ACS Catalysis, 8 (2018) 6203-6215. https://doi.org/10.1021/acscatal.7b04469